This is the author's version of an article that has been published in this journal. Changes were made to this version by the publisher prior to publication.
The final version of record is available at http://dx.doi.org/10.1109/TIP.2014.2364141

A Non-Local Structure Tensor Based Approach for Multicomponent Image Recovery Problems

Giovanni Chierchia, *Student Member, IEEE*, Nelly Pustelnik, *Member, IEEE*,
Béatrice Pesquet-Popescu, *Fellow, IEEE*, and Jean-Christophe Pesquet, *Fellow, IEEE*

***Abstract*—Non-local total variation (NLTV) has emerged as a useful tool in variational methods for image recovery problems. In this paper, we extend the NLTV-based regularization to multicomponent images by taking advantage of the structure tensor (ST) resulting from the gradient of a multicomponent image. The proposed approach allows us to penalize the non-local variations, jointly for the different components, through various $\ell_{1,p}$-matrix-norms with $p \geq 1$. To facilitate the choice of the hyper-parameters, we adopt a constrained convex optimization approach in which we minimize the data fidelity term subject to a constraint involving the ST-NLTV regularization. The resulting convex optimization problem is solved with a novel epigraphical projection method. This formulation can be efficiently implemented thanks to the flexibility offered by recent primal-dual proximal algorithms. Experiments are carried out for color, multispectral and hyperspectral images. The results demonstrate the interest of introducing a non-local structure tensor regularization and show that the proposed approach leads to significant improvements in terms of convergence speed over current state-of-the-art methods, such as the Alternating Direction Method of Multipliers.**

***Index Terms*—Convex optimization, image restoration, non-local total variation, structure tensor, singular value decomposition, hyperspectral imagery, epigraph, multicomponent images.**

I. Introduction

MULTICOMPONENT IMAGES consist of several spatial maps acquired simultaneously from a scene. Well-known examples are color images, which are composed of red, green, and blue components, or spectral images, which divide the electromagnetic spectrum into many components that represent the light intensity across a number of wavelengths. Multicomponent images are often degraded by blur and noise arising from sensor imprecisions or physical limitations, such as aperture effects, motion or atmospheric phenomena. Additionally, a decimation modelled by a sparse or random matrix can be encountered in several applications, such as compressive sensing [1]–[3], inpainting [4]–[6], or super-resolution [7]. As a consequence, the standard imaging model consists of a blurring operator [8] followed by a decimation and a (non-necessarily additive) noise.

The main focus of this paper is multicomponent image recovery from degraded observations, for which it is of paramount importance to exploit the intrinsic correlations along spatial and spectral dimensions. To this end, we adopt a variational approach based on the introduction of a *non-local total variation structure tensor* (ST-NLTV) regularization and we show how to solve it practically with constrained convex optimization techniques. In addition to more detailed theoretical developments, this paper extends our preliminary work in [9] by considering a regularization based on nuclear, Frobenius and spectral norms, by providing a performance evaluation w.r.t. two state-of-the-art methods in imaging spectroscopy [10], [11], and by presenting a comparison in terms of execution times with a solution based on the Alternating Direction Method of Multipliers method.

A. ST-NLTV regularization

The quality of the results obtained through a variational approach strongly depends on the ability to model the regularity present in images. Since natural images are often piecewise smooth, popular regularization models tend to penalize the image gradient. In this context, *total variation* (TV) [12], [13] has emerged as a simple, yet successful, convex optimization tool. However, TV fails to preserve textures, details and fine structures, because they are hardly distinguishable from noise. To improve this behaviour, the TV model has been extended by using some generalizations based on higher-order spatial differences [14], [15], higher-degree directional derivatives [16], [17], or the non-locality principle [18]–[20]. Another approach to overcome these limitations is to replace the gradient with an operator that yields a more suitable sparse representation of the image, such as a frame [21]–[26] or a learned dictionary [27]–[29]. In this context, the family of Block Matching 3-D algorithms [30], [31] has been recently formulated in terms of analysis and synthesis frames [32], substantiating the use of the non-locality principle as a valuable image modeling tool.

The extension of TV-based models to multicomponent images is, in general, non trivial. A first approach consists of computing TV channel-by-channel and then summing up the resulting smoothness measures [33]–[36]. Since there is no coupling of the components, this approach may potentially lead to component smearing and loss of edges across components. An alternative way is to process the components jointly, so

Copyright (c) 2013 IEEE. Personal use of this material is permitted. However, permission to use this material for any other purposes must be obtained from the IEEE by sending a request to pubs-permissions@ieee.org.

G. Chierchia (Corresponding author) and B. Pesquet-Popescu are with Institut Mines-Télécom, Télécom ParisTech, CNRS LTCI, 75014 Paris, France (e-mail: first.last@telecom-paristech.fr).

N. Pustelnik is with ENS Lyon, Laboratoire de Physique, UMR CNRS 5672, F69007 Lyon, France (e-mail: nelly.pustelnik@ens-lyon.fr).

J.-C. Pesquet is with Université Paris-Est, LIGM, UMR CNRS 8049, 77454 Marne-la-Vallée, France (e-mail: jean-christophe.pesquet@univ-paris-est.fr).

0000–0000/00$00.00 © 2014 IEEE

Copyright (c) 2014 IEEE. Personal use is permitted. For any other purposes, permission must be obtained from the IEEE by emailing pubs-permissions@ieee.org.

This is the author's version of an article that has been published in this journal. Changes were made to this version by the publisher prior to publication.
The final version of record is available at http://dx.doi.org/10.1109/TIP.2014.2364141

as to better reveal details and features that are not visible in each of the components considered separately. This approach naturally arises when the gradient of a multicomponent image is thought of as a *structure tensor* (ST) [37]–[45], i.e. a matrix that summarizes the prevailing direction of the gradient. The idea behind ST-based regularization is to penalize the eigenvalues of the structure tensor, in order to smooth in the direction of minimal change [33]. A concise review of both frameworks can be found in [44], where an efficient ST-TV regularization was suggested for color imagery.

In order to improve the results obtained in the color and hyperspectral restoration literature based on structure tensor, our first main contribution consists of applying the non-locality principle to ST-TV regularization.

B. Constrained formulation

Regarding the variational formulation of the data recovery problem, one may prefer to adopt a constrained formulation rather than a regularized one. Indeed, it has been recognized for a long time that incorporating constraints directly on the solution often facilitates the choice of the involved parameters [15], [46]–[51]. The constraint bounds may be related to some knowledge on the degradation process, such as the noise statistical properties, for which the expected values are known [50]. When no specific information about the noise is available, these bounds can be related to some physical properties of the target signal. For example, a reasonable upper bound on the TV constraint may be available for certain classes of images, since TV constitutes a geometrical attribute that exhibits a limited variance over, e.g., views of similar urban areas in satellite imaging, tomographic reconstructions of similar cross sections, fingerprint images, text images and face images [13].

One of the difficulties of constrained approaches is that a closed form of the projection onto the considered constraint set is not always available. Closed forms are known for convex sets such as ℓ_2-balls, hypercubes, hyperplanes, or half-spaces [52]. However, more sophisticated constraints are usually necessary in order to effectively restore multicomponent images. Taking advantage of the flexibility offered by recent proximal algorithms, we propose an epigraphical method allowing us to address a wide class of convex constraints. Our second main contribution is thus to provide an efficient solution based on proximal tools in order to solve convex problems involving matricial $\ell_{1,p}$-ball constraints.

C. Imaging spectroscopy

Spectral imagery is used in a wide range of applications, such as remote sensing [53], astronomical imaging [54], and fluorescence microscopy [55]. In these contexts, one typically distinguishes between *multispectral* (MS) and *hyperspectral* (HS) images. In general, HS images are capable to achieve a higher spectral resolution than MS images (at the cost of acquiring a few hundred bands), which results in a better spectral characterization of the objects in the scene. This gave rise to a wide array of applications in remote sensing, such as detection and identification of the ground surface [56], as well as military surveillance and historical manuscript research.

The primary characteristic of hyperspectral images is that an entire spectrum is acquired at each point, which implies a huge correlation among close spectral bands. As a result, there has been an emergence of variational methods to efficiently model the spectral-spatial regularity present in such kind of images. To the best of our knowledge, these methods can be roughly divided into three classes.

A first class of approaches consists of extending the regularity models used in color imagery [44], [57]. To cite a few examples, the work in [7] proposed a super-resolution method based on a component-by-component TV regularization. To deal with the huge size of HS images, the authors performed the actual super-resolution on a few principal image components (obtained by means of PCA), which are then used to interpolate the secondary components. In [25], the problem of MS denoising is dealt with by considering a hybrid regularization that induces each component to be sparse in an orthonormal basis, while promoting similarities between the components by means of a distance function applied on wavelet coefficients. Another kind of spectral adaptivity has been proposed in [10] for HS restoration. It consists of using the multicomponent TV regularization in [42] that averages the Frobenius norms of the multicomponent gradients. The same authors have recently proposed in [11] an inpainting method based on the multicomponent NLTV regularization. The link between this method and the proposed work will be discussed later.

A second class of approaches consists of modeling HS images as three-dimensional tensors, i.e. two spatial dimensions and one spectral dimension. First denoising attempts in this direction were pursued in [58], [59], where tensor algebra was exploited to jointly analyze the HS hypercube considering vectorial anisotropic diffusion methods. Other strategies, based on filtering, consider tensor denoising methods such as multiway Wiener filtering (see [60] for a survey on this subject).

A third class of approaches is based on robust PCA [61] or low-rank and sparse matrix decomposition [62]. These methods proceed by splitting a HS image into two separate contributions: an image formed by components having similar shapes (low-rank image) and an image that highlights the differences between the components (sparse image). For example, the work in [3] proposed a convex optimization formulation for recovering an HS image from very few compressive-sensing measurements. This approach involved a penalization based on two terms: the ℓ_* nuclear norm of the matrix where each column corresponds to the 2D-wavelet coefficients of a spectral band (reshaped in a vector) and the $\ell_{1,2}$-norm of the wavelet-coefficient blocks grouped along the spectral dimension. A similar approach was followed in [63], even though the $\ell_*/\ell_{1,2}$-norm penalization was applied directly on the HS pixels, rather than using a sparsifying linear transform.

A third contribution of this work is to adapt the proposed ST-NLTV regularization in order to efficiently deal with reconstruction problems (not only denoising) in the context of imaging spectroscopy. The resulting strategy is based on tensor algebra ideas, but it uses variational strategies rather than anisotropic diffusion or adaptive filtering. Moreover, comparisons with recent works have been performed.

Copyright (c) 2014 IEEE. Personal use is permitted. For any other purposes, permission must be obtained from the IEEE by emailing pubs-permissions@ieee.org.

This is the author's version of an article that has been published in this journal. Changes were made to this version by the publisher prior to publication.
The final version of record is available at http://dx.doi.org/10.1109/TIP.2014.2364141

D. Outline

The paper is organized as follows. Section II describes the degradation model and formulates the constrained convex optimization problem based on the non-local structure tensor. Section III explains how to minimize the corresponding objective function via proximal tools. Section IV provides an experimental validation in the context of color, MS and HS image restoration. Conclusions are given in Section V.

E. Notation

Let $\mathcal{H}$ be a real Hilbert space. $\Gamma_0(\mathcal{H})$ denotes the set of proper, lower semicontinuous, convex functions from $\mathcal{H}$ to $]-\infty,+\infty]$. Remember that a function $\varphi\colon \mathcal{H} \to]-\infty,+\infty]$ is proper if its domain $\operatorname{dom}\varphi = \big\{y \in \mathcal{H} \;\big|\; \varphi(y) < +\infty\big\}$ is nonempty. The subdifferential of φ at $x \in \mathcal{H}$ is $\partial\varphi(x) = \big\{u \in \mathcal{H} \;\big|\; (\forall y \in \mathcal{H})\ \langle y - x \mid u\rangle + \varphi(x) \leq \varphi(y)\big\}$. The epigraph of $\varphi \in \Gamma_0(\mathcal{H})$ is the nonempty closed convex subset of $\mathcal{H} \times \mathbb{R}$ defined as $\operatorname{epi}\varphi = \big\{(y,\zeta) \in \mathcal{H} \times \mathbb{R} \;\big|\; \varphi(y) \leq \zeta\big\}$, the lower level set of φ at height $\zeta \in \mathbb{R}$ is the nonempty closed convex subset of $\mathcal{H}$ defined as $\operatorname{lev}_{\leq\zeta}\varphi = \big\{y \in \mathcal{H} \;\big|\; \varphi(y) \leq \zeta\big\}$. The projection onto a nonempty closed convex subset $C \subset \mathcal{H}$ is, for every $y \in \mathcal{H}$, $P_C(y) = \operatorname{argmin}_{u\in C} \|u - y\|$. The indicator function ι_C of C is equal to 0 on C and $+\infty$ otherwise. Finally, Id (resp. Id_N) denotes the identity operator (resp. the identity matrix of size $N \times N$).

II. Proposed approach

A. Degradation model

The R-component signal of interest is denoted by $\overline{\mathrm{x}} = (\overline{x}_1, \ldots, \overline{x}_R) \in (\mathbb{R}^N)^R$. In this work, each signal component will generally correspond to an image of size $N = N_1 \times N_2$. In imaging spectroscopy, R denotes the number of spectral bands. The degradation model that we consider in this work is

$$\mathrm{z} = \mathcal{B}(\mathrm{A}\overline{\mathrm{x}}) \tag{1}$$

where $\mathrm{z} = (z_1, \ldots, z_S) \in (\mathbb{R}^K)^S$ denotes the degraded observations, $\mathcal{B}\colon (\mathbb{R}^K)^S \to (\mathbb{R}^K)^S$ models the effect of a (non-necessarily additive) noise, and $\mathrm{A} = (\mathrm{A}_{s,r})_{1\leq s\leq S, 1\leq r\leq R}$ is the degradation linear operator with $\mathrm{A}_{s,r} \in \mathbb{R}^{K\times N}$, for every $(s,r) \in \{1,\ldots,S\} \times \{1,\ldots,R\}$. In particular, this model can be specialized in some of the applications mentioned in the introduction, such as super-resolution and compressive sensing, as well as unmixing as explained in the following.

(i) **Super-resolution** [7]. In this scenario, z denotes B multicomponent images at low-resolution and $\overline{\mathrm{x}}$ denotes the (high-resolution) multicomponent image to be recovered. The operator A is a block-diagonal matrix with $S = BR$ while, for every $r \in \{1,\ldots,R\}$ and $b \in \{1,\ldots,B\}$, $\mathrm{A}_{B(r-1)+b,r} = \mathrm{D}_b\mathrm{T}\mathrm{W}_r$ is a composition of a warp matrix $\mathrm{W}_r \in \mathbb{R}^{N\times N}$, a camera blur operator $\mathrm{T} \in \mathbb{R}^{N\times N}$, and a downsampling matrix $\mathrm{D}_b \in \mathbb{R}^{K\times N}$ with $K < N$. The noise is assumed to be a zero-mean white Gaussian additive noise. It follows that B different noisy decimated versions of the same blurred and warped component are available. This yields the following degradation model: for every $r \in \{1,\ldots,R\}$ and $b \in \{1,\ldots,B\}$,

$$z_{B(r-1)+b} = \mathrm{D}_b\mathrm{T}\mathrm{W}_r\,\overline{x}_r + \varepsilon_{B(r-1)+b} \tag{2}$$

where $\varepsilon_{B(r-1)+b} \sim \mathcal{N}(0, \sigma^2\,\mathrm{Id}_K)$.

(ii) **Compressive sensing** [3]. In this scenario, z denotes the *compressed* multicomponent image and $\overline{\mathrm{x}}$ is the multicomponent image to be reconstructed. The operator A is a block-diagonal matrix where $S = R$, for every $r \in \{1,\ldots,R\}$, $\mathrm{A}_{r,r} = \mathrm{D}_r$, and $\mathrm{D}_r \in \mathbb{R}^{K\times N}$ is a random measurement matrix with $K \ll N$. The noise is assumed to be a zero-mean white Gaussian additive noise. This leads to the following degradation model:

$$(\forall r \in \{1,\ldots,R\}) \qquad z_r = \mathrm{D}_r\,\overline{x}_r + \varepsilon_r \tag{3}$$

where $\varepsilon_r \sim \mathcal{N}(0, \sigma^2\,\mathrm{Id}_K)$.

(iii) **Unmixing** [64]–[66]. In this scenario, z models an HS image with $K = N$ having several components whose spectra, denoted by $(\mathrm{S}_r)_{1\leq r\leq R} \in (\mathbb{R}^S)^R$, are supposed to be known. The goal is to determine the abundance maps of each component, thus the unknown $\overline{\mathrm{x}}$ models these abundance maps. R denotes the number of components and S the number of spectral measurements. The matrix A has a block diagonal structure that leads to the following mixing model: for every $\ell \in \{1,\ldots,N\}$,

$$\begin{bmatrix} z_1^{(\ell)} \\ \vdots \\ z_S^{(\ell)} \end{bmatrix} = \sum_{r=1}^{R} x_r^{(\ell)}\mathrm{S}_r + \varepsilon^{(\ell)}, \tag{4}$$

where $x_r^{(\ell)}$ is the pixel value for the r-th component, $z_s^{(\ell)}$ is the pixel value for the s-th spectral measurement, and $\varepsilon^{(\ell)} \sim \mathcal{N}(0, \sigma^2\,\mathrm{Id}_S)$ denotes the additive noise. In this work however, we will not focus on hyperspectral unmixing that constitutes a specific application area for which tailored algorithms have been developed.

B. Convex optimization problem

A usual solution to recover $\overline{\mathrm{x}}$ from the observations z is to follow a convex variational approach that leads to solving an optimization problem such as

$$\underset{\mathrm{x}\in C}{\text{minimize}}\ \ f(\mathrm{Ax}, \mathrm{z}) \quad \text{s.t.} \quad g(\mathrm{x}) \leq \eta, \tag{5}$$

where $\eta > 0$. The cost function $f(\cdot, \mathrm{z}) \in \Gamma_0\big((\mathbb{R}^K)^S\big)$ aims at insuring that the solution is *close to* the observations. This data term is related to the noise characteristics. For instance, standard choices for f are a quadratic function for an additive Gaussian noise, an ℓ_1-norm when a Laplacian noise is involved, and a Kullback-Leibler divergence when dealing with Poisson noise. The function $g \in \Gamma_0\big((\mathbb{R}^N)^R\big)$ allows us to impose some regularity on the solution. Some possible choices for this function have been mentioned in the introduction. Finally, C denotes a nonempty closed convex subset of $(\mathbb{R}^N)^R$ that can be used to constrain the dynamic range of the target signal, e.g. $C = ([0,255]^N)^R$ for standard natural images.

Copyright (c) 2014 IEEE. Personal use is permitted. For any other purposes, permission must be obtained from the IEEE by emailing pubs-permissions@ieee.org.

This is the author's version of an article that has been published in this journal. Changes were made to this version by the publisher prior to publication.
The final version of record is available at http://dx.doi.org/10.1109/TIP.2014.2364141

Note that state-of-the-art methods often deal with the regularized version of Problem (5), that is

$$\underset{\mathrm{x}\in C}{\text{minimize}}\ \ f(\mathrm{Ax},\mathrm{z})+\lambda g(\mathrm{x}), \tag{6}$$

where $\lambda > 0$. Actually, both formulations are equivalent for some specific values of λ and η. As mentioned in the introduction, the advantage of the constrained formulation is that the choice of η may be easier, since it is directly related to the properties of the signal to be recovered.

C. Structure Tensor regularization

In this work, we propose to model the spatial *and* spectral dependencies in multicomponent images by introducing a regularization grounded on the use of a *matrix norm*, which is defined as

$$\left(\forall \mathrm{x}\in(\mathbb{R}^N)^R\right)\qquad g(\mathrm{x})=\sum_{\ell=1}^{N}\tau_\ell\|\mathrm{F}_\ell\mathrm{B}_\ell\mathrm{x}\|_p, \tag{7}$$

where $\|\cdot\|_p$ denotes the Schatten p-norm with $p\geq 1$, $(\tau_\ell)_{1\leq\ell\leq N}$ are positive weights, and, for every $\ell\in\{1,\ldots,N\}$,

(i) **block selection**: the operator $\mathrm{B}_\ell\colon(\mathbb{R}^N)^R\to\mathbb{R}^{Q^2\times R}$ selects $Q\times Q$ blocks of each component (including the pixel ℓ) and rearranges them in a matrix of size $Q^2\times R$, so leading to

$$\mathrm{Y}^{(\ell)}=\begin{bmatrix} x_1^{(n_{\ell,1})} & \ldots & x_R^{(n_{\ell,1})}\\ \vdots & & \vdots\\ x_1^{(n_{\ell,Q^2})} & \ldots & x_R^{(n_{\ell,Q^2})}\end{bmatrix} \tag{8}$$

where $\mathcal{W}_\ell=\{n_{\ell,1},\ldots,n_{\ell,Q^2}\}$ is the set of positions located into the window around ℓ, and $Q>1$;[1]

(ii) **block transform**: the operator $\mathrm{F}_\ell\colon\mathbb{R}^{Q^2\times R}\to\mathbb{R}^{M_\ell\times R}$ denotes an analysis transform that achieves a sparse representation of grouped blocks, yielding

$$\mathrm{X}^{(\ell)}=\mathrm{F}_\ell\mathrm{Y}^{(\ell)}, \tag{9}$$

where $M_\ell\leq Q^2$.

The resulting structure tensor regularization reads

$$g(\mathrm{x})=\sum_{\ell=1}^{N}\tau_\ell\,\|\mathrm{X}^{(\ell)}\|_p. \tag{10}$$

Let us denote by

$$\sigma_{\mathrm{X}^{(\ell)}}=\left(\sigma_{\mathrm{X}^{(\ell)}}^{(m)}\right)_{1\leq m\leq\widetilde{M}_\ell},\quad\text{with }\widetilde{M}_\ell=\min\{M_\ell,R\}, \tag{11}$$

the singular values of $\mathrm{X}^{(\ell)}$ ordered in decreasing order. When $p\in[1,+\infty[$, we have

$$g(\mathrm{x})=\sum_{\ell=1}^{N}\tau_\ell\left(\sum_{m=1}^{\widetilde{M}_\ell}\left(\sigma_{\mathrm{X}^{(\ell)}}^{(m)}\right)^p\right)^{1/p}, \tag{12}$$

whereas, when $p=+\infty$,

$$g(\mathrm{x})=\sum_{\ell=1}^{N}\tau_\ell\,\sigma_{\mathrm{X}^{(\ell)}}^{(1)}. \tag{13}$$

[1]The image borders are handled through symmetric extension.

When $p=1$, the Schatten norm reduces to the nuclear norm. In such a case, the structure tensor regularization induces a low-rank approximation of matrices $(\mathrm{X}^{(\ell)})_{1\leq\ell\leq N}$ (see [67] for a survey on singular value decomposition).

The structure tensor regularization proposed in (9) generalizes several state-of-the-art regularization strategies, as explained in the following.

1) ST-TV : We retrieve the multicomponent TV regularization [10], [42], [44] by setting F_ℓ to the operator which, for each component index $r\in\{1,\ldots,R\}$, computes the difference between $x_r^{(\ell)}$ and its horizontal/vertical nearest neighbours $(x_r^{(\ell_1)},x_r^{(\ell_2)})$, yielding the matrix

$$\mathrm{X}_{\mathrm{TV}}^{(\ell)}=\begin{bmatrix} x_1^{(\ell)}-x_1^{(\ell_1)} & \ldots & x_R^{(\ell)}-x_R^{(\ell_1)}\\ x_1^{(\ell)}-x_1^{(\ell_2)} & \ldots & x_R^{(\ell)}-x_R^{(\ell_2)}\end{bmatrix} \tag{14}$$

with $M_\ell=2$. This implies a 2×2 block selection operator (i.e., $Q=2$). Special cases of ST-TV regularization can be found in the literature when $p=2$ [10], or when $F_\ell=\mathrm{Id}$ and $p=1$ [68]. We will refer to the regularization in [10] as Hyperspectral-TV in Section IV. Moreover, the regularization in [45] can be seen as an extension of ST-TV arising by setting $\mathrm{X}^{(\ell)}=[\mathrm{X}_{\mathrm{TV}}^{(n)}]_{n\in\mathcal{W}_\ell}$, yielding a matrix of size $2\times RQ^2$ (see below (8) for the definition of $\mathcal{W}_\ell$). Finally, note that the regularization used in [7] is intrinsically different from ST-TV, as the former amounts to summing up the smoothed TV [69] evaluated separately over each component.

2) ST-NLTV: We extend the NLTV regularization [18] to multicomponent images by setting F_ℓ to the operator which, for each component index $r\in\{1,\ldots,R\}$, computes the weighted difference between $x_r^{(\ell)}$ and some other pixel values. This results in the matrix

$$\mathrm{X}_{\mathrm{NLTV}}^{(\ell)}=\left[\omega_{\ell,n}(x_r^{(\ell)}-x_r^{(n)})\right]_{n\in\mathcal{N}_\ell,1\leq r\leq R}, \tag{15}$$

where $\mathcal{N}_\ell\subset\mathcal{W}_\ell\setminus\{\ell\}$ denotes the non-local support of the neighbourhood of ℓ. Here, M_ℓ corresponds to the size of this support. Note that the regularization in [11] appears as a special case of the proposed ST-NLTV arising when $p=2$ and the local window is fully used ($M_\ell=Q^2$). We will refer to it as Multichannel-NLTV in Section IV.

For every $\ell\in\{1,\ldots,N\}$ and $n\in\mathcal{N}_\ell$, the weight $\omega_{\ell,n}>0$ depends on the similarity between patches built around the pixels ℓ and n of the image to be recovered. Since the degradation process in (1) may involve some missing data, we follow a two-step approach in order to estimate these weights. In the first step, the ST-TV regularization is used in order to obtain an estimate $\widetilde{\mathrm{x}}$ of the target image. This estimate subsequently serves in the second step to compute the weights through a *self-similarity* measure as follows:

$$\omega_{\ell,n}=\widetilde{\omega}_\ell\exp\left(-\delta^{-2}\,\|\mathrm{L}_\ell\widetilde{\mathrm{x}}-\mathrm{L}_n\widetilde{\mathrm{x}}\|_2^2\right), \tag{16}$$

where $\delta>0$, L_ℓ (resp. L_n) selects a $\widetilde{Q}\times\widetilde{Q}\times R$ patch centered at position ℓ (resp. n) after a linear processing depending on the position ℓ (resp. n), and the constant $\widetilde{\omega}_\ell>0$ is set so as to normalize the weights (i.e. $\sum_{n\in\mathcal{N}_\ell}\omega_{\ell,n}=1$). Note that the linear processing is applied to improve the reliability of the self-similarity measure, and thus to insure better image

Copyright (c) 2014 IEEE. Personal use is permitted. For any other purposes, permission must be obtained from the IEEE by emailing pubs-permissions@ieee.org.

This is the author's version of an article that has been published in this journal. Changes were made to this version by the publisher prior to publication.
The final version of record is available at http://dx.doi.org/10.1109/TIP.2014.2364141

recovery performance. In the simplest case, it consists of pointwise multiplying the selected patches by a bivariate Gaussian function [70]. A more sophisticated processing may involve a convolution with a set of low-pass Gaussian filters whose variances increase as the spatial distance from the patch center grow [71]. For every $\ell \in \{1, \ldots, N\}$, the neighbourhood $\mathcal{N}_\ell$ is built according to the procedure described in [72]. In practice, we limit the size of the neighbourhood, so that $M^{(\ell)} \leq \overline{M}$ (the choices of Q, $\widetilde{Q}$, δ and $\overline{M}$ are indicated in Section IV).

III. Optimization method

Within the proposed constrained optimization framework, Problem (5) can be reformulated as follows:

$$\underset{\mathrm{x}\in C}{\text{minimize}} \;\; f(\mathrm{Ax}, \mathrm{z}) \quad \text{s.t.} \quad \Phi\,\mathrm{x} \in D, \tag{17}$$

where Φ is the linear operator defined as

$$\Phi\colon \mathrm{x} \mapsto \mathrm{X} = \begin{bmatrix} \mathrm{F}_1\mathrm{B}_1\mathrm{x} \\ \vdots \\ \mathrm{F}_N\mathrm{B}_N\mathrm{x} \end{bmatrix} \begin{matrix} \} \, \mathrm{X}^{(1)} \\ \\ \} \, \mathrm{X}^{(N)} \end{matrix} \tag{18}$$

with $\mathrm{X} \in \mathbb{R}^{M\times R}$ and $M = M_1 + \cdots + M_N$, while D is the closed convex set defined as

$$D = \big\{\mathrm{X} \in \mathbb{R}^{M\times R} \;\big|\; \sum_{\ell=1}^{N} \tau_\ell \|\mathrm{X}^{(\ell)}\|_p \leq \eta\big\}. \tag{19}$$

In recent works, iterative procedures were proposed to deal with an $\boldsymbol{\ell}_1$- or $\boldsymbol{\ell}_{1,2}$-ball constraint [73] and an $\boldsymbol{\ell}_{1,\infty}$-ball constraint [74]. Similar techniques can be used to compute the projection onto D, but a more efficient approach consists of adapting the epigraphical splitting technique investigated in [15], [75]–[77].

A. Epigraphical splitting

Epigraphical splitting applies to a convex set that can be expressed as the lower level set of a separable convex function, such as the constraint set D defined in (19). Some auxiliary variables are introduced into the minimization problem, so that the constraint D can be *equivalently* re-expressed as the intersection of two convex sets. More specifically, different splitting solutions need to be proposed according to the involved Schatten p-norm:

(i) in the case when $p = 1$, since

$$\mathrm{X} \in D \quad \Leftrightarrow \quad \sum_{\ell=1}^{N} \sum_{m=1}^{\widetilde{M}_\ell} \tau_\ell \left|\sigma^{(m)}_{\mathrm{X}^{(\ell)}}\right| \leq \eta, \tag{20}$$

we propose to introduce an auxiliary vector $\zeta \in \mathbb{R}^{\widetilde{M}}$, with $\zeta = (\zeta^{(\ell,m)})_{1\leq\ell\leq N, 1\leq m\leq\widetilde{M}_\ell}$ and $\widetilde{M} = \widetilde{M}_1 + \ldots + \widetilde{M}_N$, in order to rewrite (20) as

$$\begin{cases} (\forall \ell \in \{1, \ldots, N\}) \\ \quad (\forall m \in \{1, \ldots, \widetilde{M}_\ell\}) \quad \left|\sigma^{(m)}_{\mathrm{X}^{(\ell)}}\right| \leq \zeta^{(\ell,m)}, \\ \displaystyle\sum_{\ell=1}^{N} \sum_{m=1}^{\widetilde{M}_\ell} \tau_\ell\, \zeta^{(\ell,m)} \leq \eta. \end{cases} \tag{21}$$

Consequently, Constraint (20) is decomposed in two convex sets: a union of epigraphs

$$E = \big\{(\mathrm{X}, \zeta) \in \mathbb{R}^{M\times R} \times \mathbb{R}^{\widetilde{M}} \;\big|\; (\forall \ell \in \{1, \ldots, N\}) \\ (\forall m \in \{1, \ldots, \widetilde{M}_\ell\}) \quad (\sigma^{(m)}_{\mathrm{X}^{(\ell)}}, \zeta^{(\ell,m)}) \in \mathrm{epi}\,|\cdot|\big\}, \tag{22}$$

and the closed half-space

$$W = \big\{\zeta \in \mathbb{R}^{\widetilde{M}} \;\big|\; \sum_{\ell=1}^{N} \sum_{m=1}^{\widetilde{M}_\ell} \tau_\ell\, \zeta^{(\ell,m)} \leq \eta\big\}. \tag{23}$$

(ii) in the case when $p > 1$, since

$$\mathrm{X} \in D \quad \Leftrightarrow \quad \sum_{\ell=1}^{N} \tau_\ell \left\|\sigma_{\mathrm{X}^{(\ell)}}\right\|_p \leq \eta, \tag{24}$$

we define an auxiliary vector $\zeta = (\zeta^{(\ell)})_{1\leq\ell\leq N} \in \mathbb{R}^N$ of *smaller* dimension N, and we rewrite Constraint (24) as

$$\begin{cases} (\forall \ell \in \{1, \ldots, N\}) \quad \left\|\sigma_{\mathrm{X}^{(\ell)}}\right\|_p \leq \zeta^{(\ell)}, \\ \displaystyle\sum_{\ell=1}^{N} \tau_\ell\, \zeta^{(\ell)} \leq \eta. \end{cases} \tag{25}$$

Similarly to the previous case, Constraint (24) is decomposed in two convex sets: a union of epigraphs

$$E = \big\{(\mathrm{X}, \zeta) \in \mathbb{R}^{M\times R} \times \mathbb{R}^{N} \;\big|\; (\forall \ell \in \{1, \ldots, N\}) \\ (\sigma_{\mathrm{X}^{(\ell)}}, \zeta^{(\ell)}) \in \mathrm{epi}\,\|\cdot\|_p\big\}, \tag{26}$$

and the closed half-space

$$W = \big\{\zeta \in \mathbb{R}^{N} \;\big|\; \sum_{\ell=1}^{N} \tau_\ell\, \zeta^{(\ell)} \leq \eta\big\}. \tag{27}$$

B. Epigraphical projection

The epigraphical splitting technique allows us to reformulate Problem (17) in a more tractable way, as follows

$$\underset{(\mathrm{x},\zeta)\in C\times W}{\text{minimize}} \;\; f(\mathrm{Ax}, \mathrm{z}) \quad \text{s.t.} \quad (\Phi\,\mathrm{x},\, \zeta) \in E. \tag{28}$$

The advantage of such a decomposition is that the projections P_E and P_W onto E and W may have closed-form expressions. Indeed, the projection P_W is well-known [78], while properties of the projection P_E are summarized in the following proposition, which is straightforwardly proved.

Proposition III.1. *For every $\ell \in \{1, \ldots, N\}$, let*

$$\mathrm{X}^{(\ell)} = \mathrm{U}^{(\ell)}\mathrm{S}^{(\ell)}\big(\mathrm{V}^{(\ell)}\big)^\top \tag{29}$$

be the Singular Value Decomposition of $\mathrm{X}^{(\ell)} \in \mathbb{R}^{M_\ell\times R}$, where

- $(\mathrm{U}^{(\ell)})^\top\mathrm{U}^{(\ell)} = \mathrm{Id}_{\widetilde{M}_\ell}$,
- $\big(\mathrm{V}^{(\ell)}\big)^\top\mathrm{V}^{(\ell)} = \mathrm{Id}_{\widetilde{M}_\ell}$,
- $\mathrm{S}^{(\ell)} = \mathrm{Diag}(\mathrm{s}^{(\ell)})$, *with* $\mathrm{s}^{(\ell)} = (\sigma^{(m)}_{\mathrm{X}^{(\ell)}})_{1\leq m\leq\widetilde{M}_\ell}$.

Then,

$$P_E(\mathrm{X}, \zeta) = \Big(\mathrm{U}^{(\ell)}\mathrm{T}^{(\ell)}\big(\mathrm{V}^{(\ell)}\big)^\top,\; \theta^{(\ell)}\Big)_{1\leq\ell\leq N}, \tag{30}$$

where $\mathrm{T}^{(\ell)} = \mathrm{Diag}(\mathrm{t}^{(\ell)})$ and,

Copyright (c) 2014 IEEE. Personal use is permitted. For any other purposes, permission must be obtained from the IEEE by emailing pubs-permissions@ieee.org.

This is the author's version of an article that has been published in this journal. Changes were made to this version by the publisher prior to publication.
The final version of record is available at http://dx.doi.org/10.1109/TIP.2014.2364141

(i) *in the case* $p = 1$*, for every* $m \in \{1, \dots, \widetilde{M}_\ell\}$

$$(\mathsf{t}^{(\ell,m)},\ \theta^{(\ell,m)}) = P_{\mathrm{epi}\,|\cdot|}(\mathsf{s}^{(\ell,m)}, \zeta^{(\ell,m)}), \tag{31}$$

(ii) *in the case* $p > 1$,

$$(\mathsf{t}^{(\ell)},\ \theta^{(\ell)}) = P_{\mathrm{epi}\,\|\cdot\|_p}(\mathsf{s}^{(\ell)}, \zeta^{(\ell)}). \tag{32}$$

The above result states that the projection onto the epigraph of the $\boldsymbol{\ell}_{1,p}$ matrix norm can be deduced from the projection onto the epigraph of the $\boldsymbol{\ell}_{1,p}$ vector norm. It turns out that closed-form expressions of the latter projection exist when $p \in \{1, 2, +\infty\}$ [75]. For example, for every $(\mathsf{s}^{(\ell)}, \zeta^{(\ell)}) \in \mathbb{R}^{\widetilde{M}_\ell} \times \mathbb{R}$,

$$P_{\mathrm{epi}\,\|\cdot\|_2}(\mathsf{s}^{(\ell)}, \zeta^{(\ell)}) = \begin{cases} (0,0), & \text{if } \|\mathsf{s}^{(\ell)}\|_2 < -\zeta^{(\ell)}, \\ (\mathsf{s}^{(\ell)}, \zeta^{(\ell)}), & \text{if } \|\mathsf{s}^{(\ell)}\|_2 < \zeta^{(\ell)}, \\ \beta^{(\ell)}\left(\mathsf{s}^{(\ell)}, \|\mathsf{s}^{(\ell)}\|_2\right), & \text{otherwise,} \end{cases} \tag{33}$$

where $\beta^{(\ell)} = \dfrac{1}{2}\left(1 + \dfrac{\zeta^{(\ell)}}{\|\mathsf{s}^{(\ell)}\|_2}\right)$. Note that the closed-form expression for $p = 1$ can be derived from (33). Moreover,

$$P_{\mathrm{epi}\,\|\cdot\|_\infty}(\mathsf{s}^{(\ell)}, \zeta^{(\ell)}) = (\mathsf{t}^{(\ell)},\ \theta^{(\ell)}), \tag{34}$$

where, for every $\mathsf{t}^{(\ell)} = (\mathsf{t}^{(\ell,m)})_{1 \leq m \leq \widetilde{M}_\ell} \in \mathbb{R}^{\widetilde{M}_\ell}$,

$$\mathsf{t}^{(\ell,m)} = \min\left\{\sigma^{(m)}_{X^{(\ell)}}, \theta^{(\ell)}\right\}, \tag{35}$$

$$\theta^{(\ell)} = \frac{\max\left\{\zeta^{(\ell)} + \sum_{k=\overline{k}_\ell}^{\widetilde{M}_\ell} \nu^{(\ell,k)}, 0\right\}}{\widetilde{M}_\ell - \overline{k}_\ell + 2}. \tag{36}$$

Hereabove, $(\nu^{(\ell,k)})_{1 \leq k \leq \widetilde{M}_\ell}$ is a sequence of real numbers obtained by sorting $(\sigma^{(m)}_{X^{(\ell)}})_{1 \leq m \leq \widetilde{M}_\ell}$ in ascending order (by setting $\nu^{(\ell,0)} = -\infty$ and $\nu^{(\ell,\widetilde{M}_\ell+1)} = +\infty$), and $\overline{k}_\ell$ is the unique integer in $\{1, \dots, \widetilde{M}_\ell + 1\}$ such that

$$\nu^{(\ell,\overline{k}_\ell - 1)} < \frac{\zeta^{(\ell)} + \sum_{k=\overline{k}_\ell}^{\widetilde{M}_\ell} \nu^{(\ell,k)}}{\widetilde{M}_\ell - \overline{k}_\ell + 2} \leq \nu^{(\ell,\overline{k}_\ell)} \tag{37}$$

(with the convention $\sum_{k=\widetilde{M}^{(\ell)}+1}^{\widetilde{M}^{(\ell)}} \cdot = 0$, i.e. the sum is equal to zero when the subscript is greater than the superscript).

Note that the computation of the SVD can be avoided when $p = 2$, as the Frobenius norm is equal to the $\boldsymbol{\ell}_2$-norm of the vector of all matrix elements.

C. Proposed algorithm

The solution of (28) requires an efficient algorithm for dealing with large scale problems involving nonsmooth functions and linear operators that are non-necessarily circulant. For this reason, we resort here to proximal algorithms [79]–[96]. The key tool in these methods is the proximity operator [97] of a function $\phi \in \Gamma_0(\mathcal{H})$ on a real Hilbert space, defined as

$$(\forall \mathrm{u} \in \mathcal{H}) \qquad \mathrm{prox}_\phi(\mathrm{u}) = \operatorname*{argmin}_{\mathrm{v} \in \mathcal{H}} \frac{1}{2}\|\mathrm{v} - \mathrm{u}\|^2 + \phi(\mathrm{v}). \tag{38}$$

The proximity operator can be interpreted as an implicit subgradient step for the function ϕ, since $\mathrm{p} = \mathrm{prox}_\phi(\mathrm{u})$ is uniquely defined through the inclusion $\mathrm{u} - \mathrm{p} \in \partial\phi(\mathrm{p})$. Proximity operators enjoy many interesting properties [80]. In particular, they generalize the notion of projection onto a closed convex set C, in the sense that $\mathrm{prox}_{\iota_C} = P_C$. Hence, proximal methods provide a unifying framework that allows one to address a wide class of convex optimization problems involving non-smooth penalizations and hard constraints.

Among the wide array of existing proximal algorithms, we employ the primal-dual M+LFBF algorithm recently proposed in [92], which is able to address general convex optimization problems involving nonsmooth functions and linear operators without requiring any matrix inversion. This algorithm is able to solve numerically:

$$\underset{\mathrm{v} \in \mathcal{H}}{\text{minimize}}\ \ \phi(\mathrm{v}) + \sum_{i=1}^{I} \psi_i(\mathrm{T}_i \mathrm{v}) + \varphi(\mathrm{v}). \tag{39}$$

where $\phi \in \Gamma_0(\mathcal{H})$, for every $i \in \{1, \dots, I\}$, $\mathrm{T}_i \colon \mathcal{H} \to \mathcal{G}_i$ is a bounded linear operator, $\psi_i \in \Gamma_0(\mathcal{G}_i)$ and $\varphi \colon \mathcal{H} \to]-\infty, +\infty]$ is a convex differentiable function with a μ-Lipschitzian gradient. Our minimization problem fits nicely into this framework by setting $\mathcal{H} = (\mathbb{R}^N)^R \times \mathbb{R}^L$ with

$$L = \begin{cases} \widetilde{M} & \text{if } p = 1, \\ N & \text{if } p > 1, \end{cases} \tag{40}$$

and $\mathrm{v} = (\mathrm{x}, \zeta)$. Indeed, we set $I = 2$, $\mathcal{G}_1 = \mathbb{R}^{M \times R} \times \mathbb{R}^L$ and $\mathcal{G}_2 = (\mathbb{R}^K)^S$ in (39), the linear operators reduce to

$$\mathrm{T}_1 = \begin{bmatrix} \Phi & 0 \\ 0 & \mathrm{Id}_L \end{bmatrix}, \qquad \mathrm{T}_2 = \begin{bmatrix} \mathrm{A} & 0 \end{bmatrix}, \tag{41}$$

and the functions are as follows

$$\begin{aligned} &(\forall (\mathrm{x}, \zeta) \in (\mathbb{R}^N)^R \times \mathbb{R}^L) && \phi(\mathrm{x}, \zeta) && = \iota_C(\mathrm{x}) + \iota_W(\zeta), \\ &(\forall (\mathrm{X}, \zeta) \in \mathbb{R}^{M \times R} \times \mathbb{R}^L) && \psi_1(\mathrm{X}, \zeta) && = \iota_E(\mathrm{X}, \zeta), \\ &(\forall \mathrm{y} \in (\mathbb{R}^K)^S) && \psi_2(\mathrm{y}) && = f(\mathrm{y}, \mathrm{z}), \\ &(\forall (\mathrm{x}, \zeta) \in (\mathbb{R}^N)^R \times \mathbb{R}^L) && \varphi(\mathrm{x}, \zeta) && = 0. \end{aligned} \tag{42}$$

The iterations associated with Problem (28) are summarized in Algorithm 1, where $\mathrm{A}^\top$ and $\Phi^\top$ designate the adjoint operators of A and Φ. The sequence $(\mathrm{x}^{[t]})_{t \in \mathbb{N}}$ generated by the algorithm is guaranteed to converge to a solution to (28) (see [92]).

D. Approach based on ADMM

Note that an alternative approach to deal with Problem (17) consists of employing the Alternating Direction Method of Multipliers (ADMM) [98] or one of its parallel versions [86], [87], [99]–[102], sometimes referred to as the Simultaneous Direction Method of Multipliers (SDMM). Although these algorithms are appealing, they require to invert the operator $\mathrm{Id} + \Phi^\top\Phi + \mathrm{A}^\top\mathrm{A}$, which makes them less attractive than primal-dual algorithms for solving Problem (17). Indeed, this matrix is not diagonalizable in the DFT domain (due to the form of Φ), which rules out efficient inversion techniques such as those employed in [100], [103], [104]. To the best of our knowledge, this issue can be circumvented in specific cases only, for example when Φ denotes the NLTV operator defined in (15). In this case, one may resort to the solution in [25],

Copyright (c) 2014 IEEE. Personal use is permitted. For any other purposes, permission must be obtained from the IEEE by emailing pubs-permissions@ieee.org.

This is the author's version of an article that has been published in this journal. Changes were made to this version by the publisher prior to publication.
The final version of record is available at http://dx.doi.org/10.1109/TIP.2014.2364141

Algorithm 1 M+LFBF for solving Problem (28)

Initialization

$\mathrm{Y}_1^{[0]} \in \mathbb{R}^{M\times R}, \nu_1^{[0]} \in \mathbb{R}^L$

$\mathrm{y}_2^{[0]} \in (\mathbb{R}^K)^S$

$\mathrm{x}^{[0]} \in (\mathbb{R}^N)^R, \zeta^{[0]} \in \mathbb{R}^L$

$\theta = \sqrt{\|\mathrm{A}\|^2 + \max\{\|\Phi\|^2, 1\}}$

$\epsilon \in]0, \frac{1}{\theta+1}[$

For $t = 0, 1, \ldots$

$\gamma_t \in \left[\epsilon, \dfrac{1-\epsilon}{\theta}\right]$

$\left(\widehat{\mathrm{x}}^{[t]}, \widehat{\zeta}^{[t]}\right) = \left(\mathrm{x}^{[t]}, \zeta^{[t]}\right) - \gamma_t\left(\Phi^\top \mathrm{Y}_1^{[t]} + \mathrm{A}^\top \mathrm{y}_2^{[t]}, \nu^{[t]}\right)$

$\left(\mathrm{p}^{[t]}, \rho^{[t]}\right) = \left(P_C(\widehat{\mathrm{x}}^{[t]}), P_W(\widehat{\zeta}^{[t]})\right)$

$\left(\widehat{\mathrm{Y}}_1^{[t]}, \widehat{\nu}_1^{[t]}\right) = \left(\mathrm{Y}_1^{[t]}, \nu_1^{[t]}\right) + \gamma_t\left(\Phi \mathrm{x}^{[t]}, \zeta^{[t]}\right)$

$\left(\widetilde{\mathrm{Y}}_1^{[t]}, \widetilde{\nu}_1^{[t]}\right) = \left(\widehat{\mathrm{Y}}_1^{[t]}, \widehat{\nu}_1^{[t]}\right) - \gamma_t P_E\left(\widehat{\mathrm{Y}}_1^{[t]}/\gamma_t, \widehat{\nu}_1^{[t]}/\gamma_t\right)$

$\left(\mathrm{Y}_1^{[t+1]}, \nu_1^{[t+1]}\right) = \left(\widetilde{\mathrm{Y}}_1^{[t]}, \widetilde{\nu}_1^{[t]}\right) + \gamma_t\left(\Phi(\mathrm{p}^{[t]} - \mathrm{x}^{[t]}), \rho^{[t]} - \zeta^{[t]}\right)$

$\widehat{\mathrm{y}}_2^{[t]} = \mathrm{y}_2^{[t]} + \gamma_t \mathrm{A}\mathrm{x}^{[t]}$

$\widetilde{\mathrm{y}}_2^{[t]} = \widehat{\mathrm{y}}_2^{[t]} - \gamma_t \operatorname{prox}_{\gamma_t^{-1} f}\left(\widehat{\mathrm{y}}_2^{[t]}/\gamma_t\right)$

$\mathrm{y}_2^{[t+1]} = \widetilde{\mathrm{y}}_2^{[t]} + \gamma_t \mathrm{A}(\mathrm{p}^{[t]} - \mathrm{x}^{[t]})$

$\left(\widetilde{\mathrm{x}}^{[t]}, \widetilde{\zeta}^{[t]}\right) = \left(\mathrm{p}^{[t]}, \rho^{[t]}\right) - \gamma_t\left(\Phi^\top \widetilde{\mathrm{Y}}_1^{[t]} + \mathrm{A}^\top \widetilde{\mathrm{y}}_2^{[t]}, \widetilde{\nu}_1^{[t]}\right)$

$\left(\mathrm{x}^{[t+1]}, \zeta^{[t+1]}\right) = \left(\mathrm{x}^{[t]} - \widehat{\mathrm{x}}^{[t]} + \widetilde{\mathrm{x}}^{[t]}, \zeta^{[t]} - \widehat{\zeta}^{[t]} + \widetilde{\zeta}^{[t]}\right)$

[105], which consists of decomposing Φ as follows:

$$\Phi = \Omega \underbrace{\begin{bmatrix} \mathrm{G}_1 \\ \vdots \\ \mathrm{G}_{Q^2-1} \end{bmatrix}}_{\mathrm{G}}, \tag{43}$$

where, for every $q \in \{1, \ldots, Q^2-1\}$, $\mathrm{G}_q \colon (\mathbb{R}^N)^R \to \mathbb{R}^{N\times R}$ is a discrete difference operator and $\Omega \in \mathbb{R}^{M\times N(Q^2-1)}$ is a weighted block-selection operator. So doing, Problem (17) can be *equivalently* reformulated by introducing an auxiliary variable $\xi = \Phi \mathrm{x} \in \mathbb{R}^{M\times R}$, yielding

$$\underset{(\mathrm{x},\xi)\in C\times D}{\text{minimize}} \; f(\mathrm{A}\mathrm{x}, \mathrm{z}) \quad \text{s.t.} \quad (\mathrm{G}\mathrm{x}, \xi) \in V, \tag{44}$$

where $V = \left\{(\mathrm{X}, \xi) \in \mathbb{R}^{N(Q^2-1)\times R} \times \mathbb{R}^{M\times R} \;\middle|\; \Omega \mathrm{X} = \xi\right\}$. The iterations associated to SDMM are illustrated in Algorithm 2.

It is worth emphasizing that SDMM still requires to compute the projection onto D, which may be done by either resorting to specific numerical solutions [73], [74], [106], [107] or employing the epigraphical splitting technique presented in Section III-A. However, according to our simulations (see Section IV-C), both approaches are slower than Algorithm 1.

IV. Numerical results

A. Color photography

In this section, we numerically evaluate the ST-NLTV regularization proposed in Section II and compare it with a standard *channel-by-channel* (CC) regularization [34], [75]:

$$g_{\mathrm{cc}}(\mathrm{x}) = \sum_{r=1}^{R}\sum_{\ell=1}^{N} \tau_\ell \|X_r^{(\ell)}\|_p, \tag{45}$$

Algorithm 2 SDMM for solving Problem (44)

Initialization

$\mathrm{y}_1^{[0]} \in (\mathbb{R}^N)^R, \mathrm{Y}_2^{[0]} \in \mathbb{R}^{M\times R}, \mathrm{y}_3^{[0]} \in (\mathbb{R}^K)^S$

$\overline{\mathrm{y}}_1^{[0]} \in (\mathbb{R}^N)^R, \overline{\mathrm{Y}}_2^{[0]} \in \mathbb{R}^{M\times R}, \overline{\mathrm{y}}_3^{[0]} \in (\mathbb{R}^K)^S$

$\chi_1^{[0]} \in \mathbb{R}^{M\times R}, \chi_2^{[0]} \in \mathbb{R}^{M\times R}$

$\overline{\chi}_1^{[0]} \in \mathbb{R}^{M\times R}, \overline{\chi}_2^{[0]} \in \mathbb{R}^{M\times R}$

$\mathrm{H} = \mathrm{Id} + \mathrm{G}^\top \mathrm{G} + \mathrm{A}^\top \mathrm{A}$

For $t = 0, 1, \ldots$

$\gamma_t \in]0, +\infty[$

$\mathrm{x}^{[t]} = \mathrm{H}^{-1}\left[\mathrm{y}_1^{[t]} - \overline{\mathrm{y}}_1^{[t]} + \mathrm{G}^\top(\mathrm{Y}_2^{[t]} - \overline{\mathrm{Y}}_2^{[t]}) + \mathrm{A}^\top(\mathrm{y}_3^{[t]} - \overline{\mathrm{y}}_3^{[t]})\right]$

$\xi^{[t]} = \frac{1}{2}\left(\chi_1^{[t]} - \overline{\chi}_1^{[t]}\right) + \frac{1}{2}\left(\chi_2^{[t]} - \overline{\chi}_2^{[t]}\right)$

$\mathrm{y}_1^{[t+1]} = P_C\left(\mathrm{x}^{[t]} + \overline{\mathrm{y}}_1^{[t]}\right)$

$\chi_1^{[t+1]} = P_D\left(\xi^{[t]} + \overline{\chi}_1^{[t]}\right)$

$\left(\mathrm{Y}_2^{[t+1]}, \chi_2^{[t+1]}\right) = P_V(\mathrm{G}\mathrm{x}^{[t]} + \overline{\mathrm{Y}}_2^{[t]}, \xi^{[t]} + \overline{\chi}_2^{[t]})$

$\mathrm{y}_3^{[t+1]} = \operatorname{prox}_{\gamma_t f}\left(\mathrm{A}\mathrm{x}^{[t]} + \overline{\mathrm{y}}_3^{[t]}\right)$

$\overline{\mathrm{y}}_1^{[t+1]} = \overline{\mathrm{y}}_1^{[t]} + \mathrm{x}^{[t]} - \mathrm{y}_1^{[t+1]}$

$\overline{\chi}_1^{[t+1]} = \overline{\chi}_1^{[t]} + \xi^{[t]} - \chi_1^{[t+1]}$

$\left(\overline{\mathrm{Y}}_2^{[t+1]}, \overline{\chi}_2^{[t+1]}\right) = \left(\overline{\mathrm{Y}}_2^{[t]} + \mathrm{G}\mathrm{x}^{[t]} - \mathrm{Y}_2^{[t+1]}, \overline{\chi}_2^{[t]} + \xi^{[t]} - \chi_2^{[t+1]}\right)$

$\overline{\mathrm{y}}_3^{[t+1]} = \overline{\mathrm{y}}_3^{[t]} + \mathrm{A}\mathrm{x}^{[t]} - \mathrm{y}_3^{[t+1]}$

where $X_r^{(\ell)}$ denotes the r-th column vector of matrix $\mathrm{X}^{(\ell)}$ defined in (9). Note that, for both CC-NLTV and ST-NLTV, we set $\tau_\ell \equiv 1$, $Q = 11$, $\widetilde{Q} = 5$, $\delta = 35$ and $\overline{M} = 14$, as this setting was observed to yield the best numerical results.

The first experiment is focused on color imaging, i.e. the case $R = S = 3$. The noisy observations are obtained with the degradation model in (3), where the measurement operator $(\mathrm{D}_r)_{1\le r\le R}$ denotes a decimated convolution. While it is common for color imaging to work in a luminance-chrominance space [108], [109], or a perceptually-uniform space [44], the random decimation prevents us from following this approach, because pixels having missing colors cannot be correctly projected onto a different color space. The experiments are thus conducted in the RGB color space, and the dynamic range constraint set C imposes that the pixel values belong to $[0, 255]$. Moreover, the fidelity term related to the noise log-likelihood is $f = \|\mathrm{A}\cdot - \mathrm{z}\|_2^2$.

In the example of Fig. 1, we collect the images reconstructed by using ℓ_p-CC-TV [34], ℓ_p-CC-NLTV [75], ℓ_p-ST-TV [42], [44] and the proposed ℓ_p-ST-NLTV for $p \in \{1, 2, +\infty\}$. The results demonstrate the interest of considering non-local structure tensor measures, ℓ_1-ST-NLTV being the most effective regularization. Indeed, ST-NLTV regularization combines the advantages of both ST and NLTV, as one can see a better preservation of details and a reduction of color smearing.

B. Imaging spectroscopy

In this section, we compare ℓ_1-ST-NLTV with implementations of two state-of-the-art methods in spectral imagery: Hyperspectral TV (H-TV) [10] (see Section II-C1), and Multichannel NLTV (M-NLTV) [11] (see Section II-C2). To this end, two scenarios are addressed by using the degradation model in (3): a compressive-sensing scenario in which the measurement operator $(\mathrm{D}_r)_{1\le r\le R}$ is a random decimation,

Copyright (c) 2014 IEEE. Personal use is permitted. For any other purposes, permission must be obtained from the IEEE by emailing pubs-permissions@ieee.org.

This is the author's version of an article that has been published in this journal. Changes were made to this version by the publisher prior to publication.
The final version of record is available at http://dx.doi.org/10.1109/TIP.2014.2364141

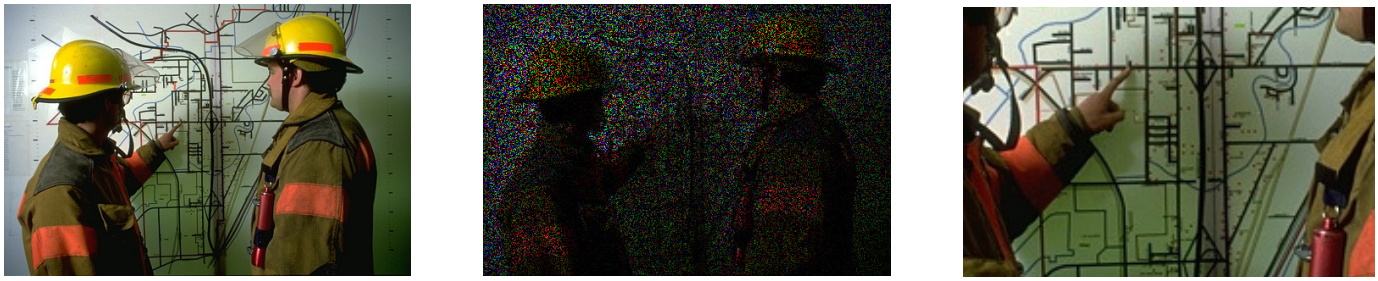

(a) Original. (b) Noisy. (c) Zoom.

(d) ℓ_1-CC-TV [34]: 16.15 dB. (e) ℓ_2-CC-TV [34]: 16.32 dB. (f) ℓ_∞-CC-TV [34]: 16.05 dB.

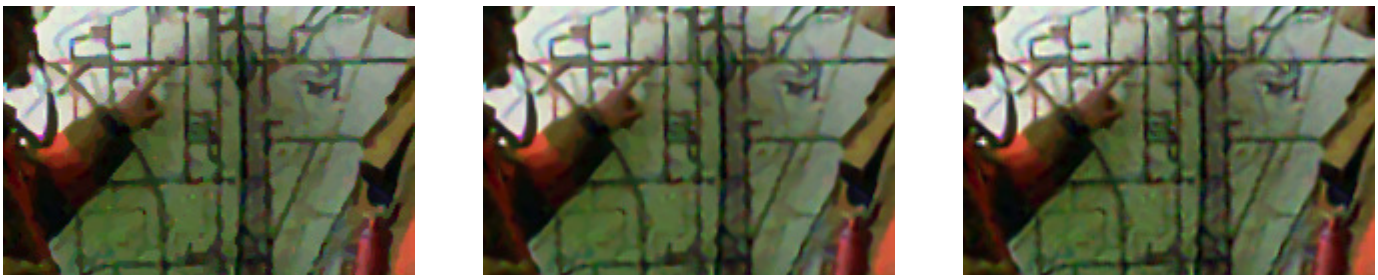

(g) ℓ_1-CC-NLTV [75]: 16.87 dB. (h) ℓ_2-CC-NLTV [75]: 17.20 dB. (i) ℓ_∞-CC-NLTV [75]: 17.22 dB.

(j) ℓ_1-ST-TV: 17.08 dB. (k) ℓ_2-ST-TV [42]: 16.84 dB. (l) ℓ_∞-ST-TV [44]: 16.43 dB.

(m) **ℓ_1-ST-NLTV: 18.20 dB.** (n) ℓ_2-ST-NLTV: 17.46 dB. (o) ℓ_∞-ST-NLTV: 16.67 dB.

Fig. 1. Visual comparison of a color image reconstructed with various regularization constraints. Degradation: additive zero-mean white Gaussian noise with std. deviation equal to 10, uniform blur of size 3×3, and 80% of decimation ($N = 154401$, $R = S = 3$ and $K = 30880$).

Copyright (c) 2014 IEEE. Personal use is permitted. For any other purposes, permission must be obtained from the IEEE by emailing pubs-permissions@ieee.org.

This is the author's version of an article that has been published in this journal. Changes were made to this version by the publisher prior to publication.
The final version of record is available at http://dx.doi.org/10.1109/TIP.2014.2364141

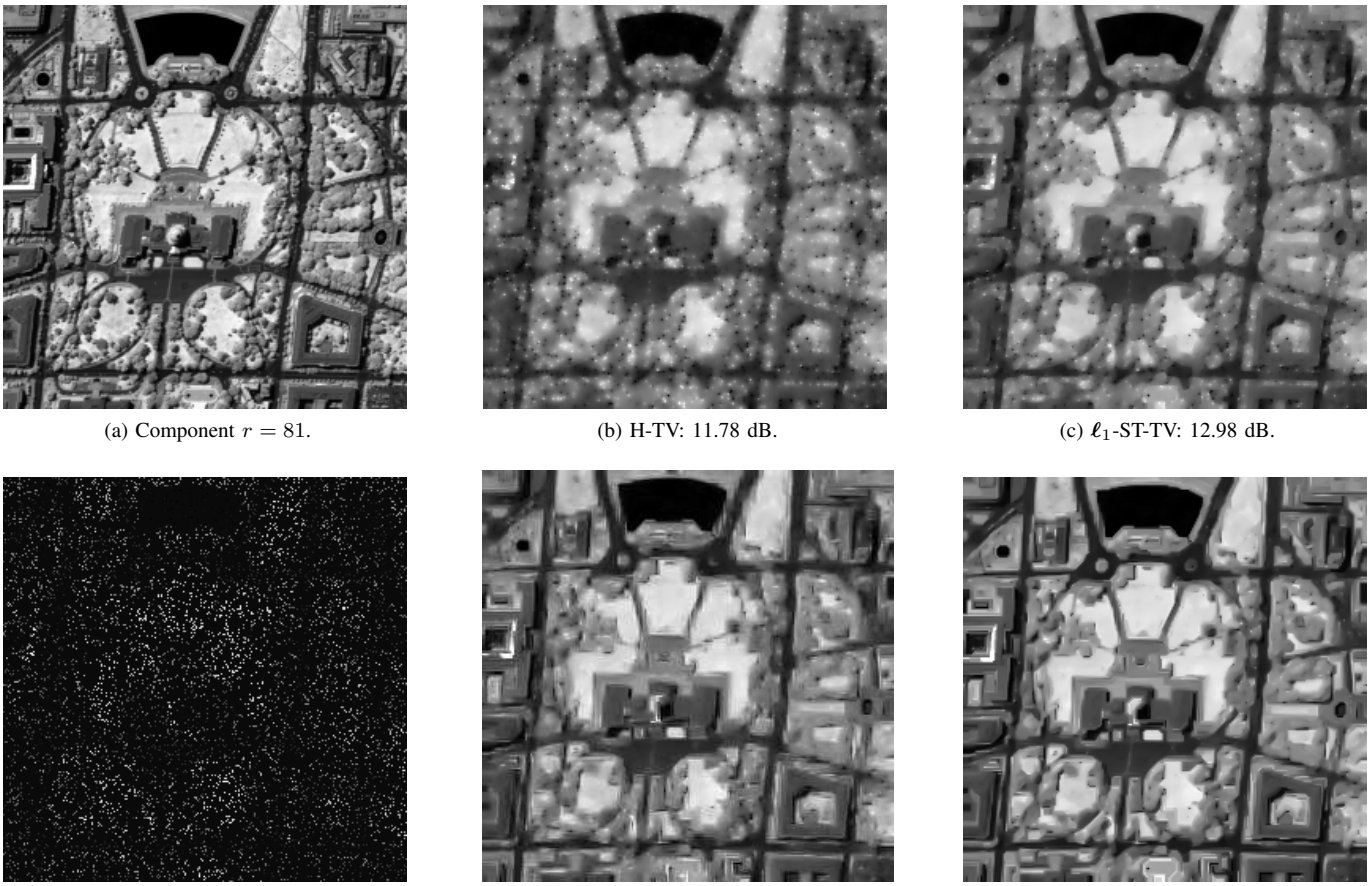

(a) Component $r = 81$. (b) H-TV: 11.78 dB. (c) ℓ_1-ST-TV: 12.98 dB.

(d) Noisy. (e) M-NLTV: 12.76 dB. (f) **ℓ_1-ST-NLTV: 14.36 dB**.

Fig. 2. Visual comparison of the hyperspectral image *hydice* reconstructed with H-TV [10], ℓ_1-ST-TV, M-NLTV [11] and ℓ_1-ST-NLTV. Degradation: compressive sensing scenario involving an additive zero-mean white Gaussian noise with std. deviation 5 and 90% of decimation ($N = 65536$, $R = 191$, $K = 6553$ and $S = 191$).

TABLE I
SNR (dB) – MEAN SNR (dB) OF RECONSTRUCTED IMAGES (DEGRADATION: STD. DEVIATION = 5, DECIMATION = 90%).

image	size	H-TV [10]	ℓ_1-ST-TV	M-NLTV [11]	ℓ_1-ST-NLTV
Hydice	$256 \times 256 \times 191$	10.65 – 09.87	11.93 – 11.16	11.57 – 10.76	**12.98 – 12.11**
Indian Pine	$145 \times 145 \times 200$	17.31 – 17.00	18.46 – 18.24	17.62 – 17.34	**19.53 – 19.49**
Little Coriver	$512 \times 512 \times 7$	17.81 – 18.20	18.49 – 18.83	18.46 – 18.90	**19.88 – 20.18**
Mississippi	$512 \times 512 \times 7$	18.27 – 18.07	18.60 – 18.37	18.94 – 18.59	**19.56 – 19.28**
Montana	$512 \times 512 \times 7$	22.49 – 20.97	22.68 – 21.15	22.85 – 21.29	**23.31 – 21.76**
Rio	$512 \times 512 \times 7$	16.48 – 15.29	16.65 – 15.48	16.82 – 15.64	**17.20 – 16.05**
Paris	$512 \times 512 \times 7$	14.85 – 14.31	14.94 – 14.39	15.05 – 14.53	**15.36 – 14.82**

TABLE II
SNR (dB) – MEAN SNR (dB) OF RESTORED IMAGES (DEGRADATION: STD. DEVIATION = 5, BLUR = 5×5, DECIMATION = 70%).

image	size	H-TV [10]	ℓ_1-ST-TV	M-NLTV [11]	ℓ_1-ST-NLTV
Hydice	$256 \times 256 \times 191$	13.76 – 12.90	14.30 – 13.50	13.84 – 12.98	**14.84 – 14.08**
Indian Pine	$145 \times 145 \times 200$	19.80 – 19.65	20.22 – 20.13	19.73 – 19.57	**20.43 – 20.41**
Little Coriver	$512 \times 512 \times 7$	21.35 – 21.88	21.62 – 22.01	21.31 – 22.00	**21.99 – 22.49**
Mississippi	$512 \times 512 \times 7$	21.12 – 20.29	21.21 – 20.27	21.41 – 20.52	**21.65 – 20.83**
Montana	$512 \times 512 \times 7$	24.80 – 23.37	24.82 – 23.31	24.96 – 23.53	**25.18 – 23.72**
Rio	$512 \times 512 \times 7$	18.62 – 17.50	18.57 – 17.48	18.57 – 17.60	**18.87 – 17.80**
Paris	$512 \times 512 \times 7$	16.68 – 16.55	16.80 – 16.53	16.73 – 16.60	**17.05 – 16.81**

Copyright (c) 2014 IEEE. Personal use is permitted. For any other purposes, permission must be obtained from the IEEE by emailing pubs-permissions@ieee.org.

This is the author's version of an article that has been published in this journal. Changes were made to this version by the publisher prior to publication.
The final version of record is available at http://dx.doi.org/10.1109/TIP.2014.2364141

and a restoration scenario in which $(\mathrm{D}_r)_{1\leq r\leq R}$ is a decimated convolution. For reproducibility purposes, we use several publicly available multispectral and hyperspectral images.[2] The SNR index is used to give a quantitative assessment of the results obtained from the simulated experiments, reporting both the SNR computed over all the image and the average of SNR indices evaluated component-by-component (M-SNR).

In our experiments, the fidelity term related to the noise log-likelihood is $f = \|\mathrm{A}\cdot - \mathrm{z}\|_2^2$. Before degrading the original images, the pixels of each component are normalized in $[0, 255]$, hence the dynamic range constraint set C imposes that the pixel values belong to $[0, 255]$. For the ST-NLTV constraints, we set $\tau_\ell \equiv 1$, $Q = 11$, $\tilde{Q} = 5$, $\delta = 35$ and $\overline{M} = 14$.

Extensive tests have been carried out on several images of different sizes. The SNR and M-SNR indices obtained by using the proposed ℓ_1-ST-TV and ℓ_1-ST-NLTV regularization constraints are collected in Tables I and II for the two degradation scenarios mentioned above. In addition, a comparison is performed between our method and the H-TV and M-NLTV algorithms mentioned above (using an M+LFBF implementation). The hyper-parameter for each method (the bound η for the ST constraint in our algorithm) was hand-tuned in order to achieve the best SNR values. The best results are highlighted in bold. Moreover, a component-by-component comparison of two hyperspectral images is made in Fig. 3, while a visual comparison of a component from the image *hydice* is displayed in Fig. 2.

The aforementioned results demonstrate the interest of combining the non-locality principle with structure-tensor smoothness measures. Indeed, ℓ_1-ST-NLTV proves to be the most effective regularization with gains in SNR (up to 1.4 dB) with respect to M-NLTV, which in turn is comparable with ℓ_1-ST-TV. The better performance of ℓ_1-ST-NLTV seems to be related to its ability to better preserve edges and thin structures present in images, while preventing component smearing.

C. Comparison with SDMM

To complete our analysis, we compare the execution time of Algorithm 1 with respect to three alternative solutions:

- M+LFBF applied to Problem (17) by computing the projection onto D via the procedure in [73];
- SDMM applied to Problem (44) by computing the projection onto D via the procedure in [73] (Algorithm 2);
- SDMM applied to Problem (44) after that the constraint D is replaced by the constraints E and W.

We would like to emphasize that all the above algorithms solve *exactly* Problem (17), hence they produce equivalent results (i.e. they converge to the same solution). Our objective here is to empirically demonstrate that the epigraphical splitting technique and primal-dual proximal algorithms constitute a competitive choice for the problem at hand.

We present the results obtained with the image *indian pine*, since a similar behaviour was observed for other images. The stopping criterion is set to $\|x^{[i+1]} - x^{[i]}\| \leq 10^{-5}\|x^{[i]}\|$. We developed in MATLAB the basic structure of the aforementioned algorithms, while the most "complex" operations (such as the non-local gradient and projection computations) were implemented in C using mex files. In order to compute the projection onto D, we used the ℓ_1-ball projector described in [73, Algorithm 2],[3] as it avoids the expensive sorting operation (a review of several ℓ_1-ball projectors can be found in [110]). Our codes were executed in Matlab R2011b with an Intel Xeon CPU at 2.80 GHz and 8 GB of RAM.

Fig. 4 shows the relative error $\|x^{[i]} - x^{[\infty]}\|/\|x^{[\infty]}\|$ as a function of the computational time, where $x^{[\infty]}$ denotes the solution computed with a stopping criterion of 10^{-5}. These plots indicate that the epigraphical approach yields a faster convergence than the direct one for both SDMM and M+LFBF, the latter being much faster than the former. This can be explained by the computational cost of the subiterations required by the direct projection onto the ℓ_1-ball. Note that these conclusions extend to all images in the dataset.

The results in Fig. 4 refer to the constraint bound η that achieves the best SNR indices. In practice, the optimal bound may not be known precisely, although a reasonable estimate may be available for certain classes of images based on statistics of databases [13]. While it is out of the scope of this paper to investigate an optimal strategy to set this bound, it is important to evaluate the impact of its choice on our method performance. In Tables III and IV, we compare the epigraphical approach with the direct computation of the projections (via standard iterative solutions) for different choices of η. For better readability, the values of η are expressed as a multiplicative factor of the ST-TV and ST-NLTV semi-norms of the original image. The execution times indicate that the epigraphical approach yields a faster convergence than the direct approach for SDMM and M+LFBF. Moreover, the numerical results show that errors within $\pm 5\%$ from the optimal value for η lead to SNR variations within 1.2%. We refer to [75] for an extensive comparison between the epigraphical and direct approaches.

V. Conclusions

We have proposed a new regularization for multicomponent images that is a combination of *non-local total variation* and *structure tensor*. The resulting image recovery problem has been formulated as a constrained convex optimization problem and solved through a novel epigraphical projection method using primal-dual proximal algorithms. The obtained results demonstrate the better performance of structure tensor and non-local gradients over a number of multispectral and hyperspectral images, although it would be interesting to consider other applications, such as the recovery of video signals or volumetric images. Our results also show that the nuclear norm has to be preferred over the Frobenius norm for hyperspectral image recovery problems. Furthermore, the experimental part indicates that the epigraphical method converges faster than the approach based on the direct computation of the projections via standard iterative solutions. In both cases, the proposed algorithm turns out to be faster than solutions based on the Alternating Direction Method of Multipliers, suggesting that primal-dual proximal algorithms constitute a good choice in practice to deal with multicomponent image recovery problems.

[2] https://engineering.purdue.edu/∼biehl/MultiSpec/hyperspectral.html

[3] The mex-file is available at `www.cs.ubc.ca/∼mpf/spgl1`

Copyright (c) 2014 IEEE. Personal use is permitted. For any other purposes, permission must be obtained from the IEEE by emailing pubs-permissions@ieee.org.

This is the author's version of an article that has been published in this journal. Changes were made to this version by the publisher prior to publication.
The final version of record is available at http://dx.doi.org/10.1109/TIP.2014.2364141

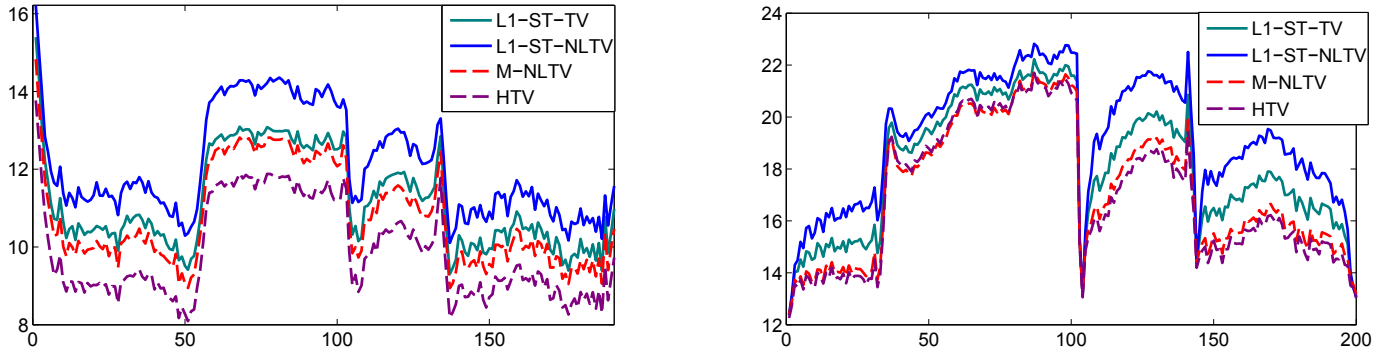

(a) SNR (dB) vs component index (image: hydice). (b) SNR (dB) vs component index (image: indian pine).

Fig. 3. Quantitative comparison of two hyperspectral images reconstructed with H-TV [10], ℓ_1-ST-TV, M-NLTV [11] and ℓ_1-ST-NLTV. Degradation: compressive sensing scenario involving an additive zero-mean white Gaussian noise with std. deviation 5 and 90% of decimation.

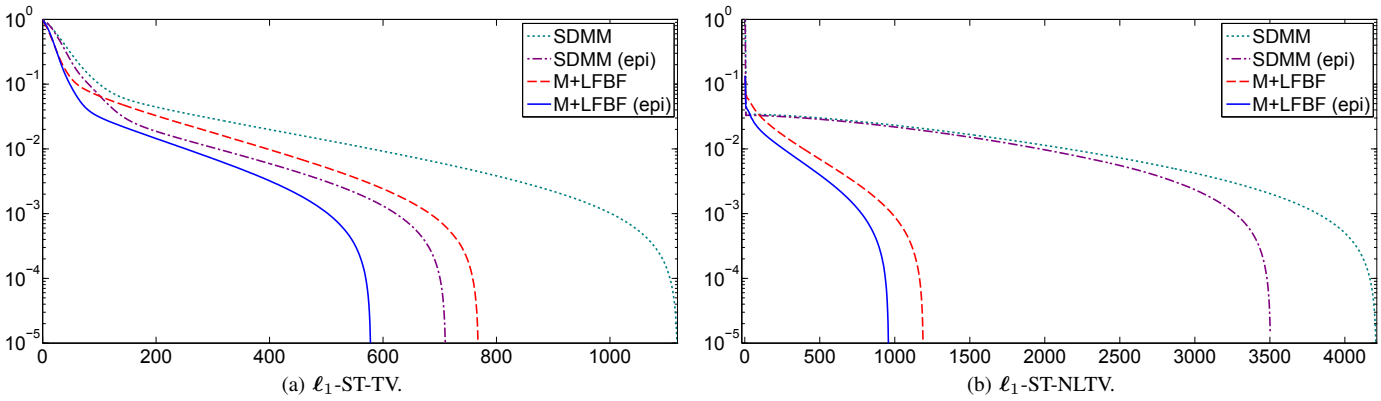

(a) ℓ_1-ST-TV. (b) ℓ_1-ST-NLTV.

Fig. 4. Comparison between epigraphical and direct methods: $\frac{\|x^{[i]}-x^{[\infty]}\|}{\|x^{[\infty]}\|}$ vs time (Degradation: std. deviation = 5, decimation = 90%).

TABLE III
RESULTS FOR THE ℓ_1-ST-TV CONSTRAINT AND SOME VALUES OF η. DEGRADATION: STD. DEVIATION = 5, DECIMATION = 90%.
("SPEED UP" IS THE RATIO BETWEEN "DIRECT" AND "EPIGRAPHICAL" TIMES)

η	SNR (dB) – M-SNR (dB)	SDMM					M+LFBF				
		direct		epigraphical		speed up	direct		epigraphical		speed up
		# iter.	sec.	# iter.	sec.		# iter.	sec.	# iter.	sec.	
0.35	18.41 – 18.19	547	767.51	471	466.80	1.64	466	471.95	389	339.24	1.39
0.40	**18.46 – 18.24**	**838**	**1066.24**	**698**	**701.03**	**1.52**	**733**	**735.36**	**621**	**558.37**	**1.32**
0.45	18.26 – 18.02	1000	1353.13	1000	990.76	1.37	1000	1018.58	1000	902.00	1.13

TABLE IV
RESULTS FOR THE ℓ_1-ST-NLTV CONSTRAINT AND SOME VALUES OF η. DEGRADATION: STD. DEVIATION = 5, DECIMATION = 90%.
("SPEED UP" IS THE RATIO BETWEEN "DIRECT" AND "EPIGRAPHICAL" TIMES)

η	SNR (dB) – M-SNR (dB)	SDMM					M+LFBF				
		direct		epigraphical		speed up	direct		epigraphical		speed up
		# iter.	sec.	# iter.	sec.		# iter.	sec.	# iter.	sec.	
		Neighbourhood size: $Q = 3$									
0.25	19.15 – 19.05	1000	4384.38	1000	3583.57	1.23	190	494.77	190	448.22	1.11
0.30	19.39 – 19.32	1000	4414.94	1000	3417.18	1.29	243	649.31	236	534.50	1.21
0.35	19.36 – 19.28	875	4175.52	1000	3482.80	1.20	319	839.86	308	726.50	1.16
		Neighbourhood size: $Q = 5$									
0.25	19.43 – 19.38	1000	14412.86	1000	10167.34	1.42	216	977.95	212	871.80	1.12
0.30	**19.55 – 19.51**	**1000**	**14338.36**	**1000**	**10174.68**	**1.41**	**275**	**1257.71**	**268**	**1143.35**	**1.10**
0.35	19.53 – 19.49	1000	14365.92	1000	10356.73	1.39	358	1631.17	347	1424.72	1.14

Copyright (c) 2014 IEEE. Personal use is permitted. For any other purposes, permission must be obtained from the IEEE by emailing pubs-permissions@ieee.org.

This is the author's version of an article that has been published in this journal. Changes were made to this version by the publisher prior to publication.
The final version of record is available at http://dx.doi.org/10.1109/TIP.2014.2364141

REFERENCES

[1] H. Rauhut, K. Schnass, and P. Vandergheynst, "Compressed sensing and redundant dictionaries," *IEEE Trans. Inform. Theory*, vol. 54, no. 5, pp. 2210–2219, May 2008.

[2] J. Romberg, "Compressive sensing by random convolution," *SIAM J. on Imaging Sci.*, vol. 2, no. 4, pp. 1098–1128, Oct. 2009.

[3] M. Golbabaee and P. Vandergheynst, "Hyperspectral image compressed sensing via low-rank and joint-sparse matrix recovery," in *Proc. Int. Conf. Acoust., Speech Signal Process.*, Kyoto, Japan, Mar. 2012.

[4] M. J. Fadili, J.-L. Starck, and F. Murtagh, "Inpainting and zooming using sparse representations," *The computer journal*, vol. 52, no. 1, pp. 64–79, Jan. 2009.

[5] L. Lorenzi, F. Melgani, and G. Mercier, "Missing-area reconstruction in multispectral images under a compressive sensing perspective," *IEEE Trans. Geosci. Remote Sens.*, vol. 51, no. 7, pp. 3998–4008, July 2013.

[6] H. Shen, X. Li, L. Zhang, D. Tao, and C. Zeng, "Compressed sensing-based inpainting of aqua moderate resolution imaging spectroradiometer band 6 using adaptive spectrum-weighted sparse bayesian dictionary learning," *IEEE Trans. Geosci. Remote Sens.*, vol. 52, no. 2, pp. 894–906, Feb. 2014.

[7] H. Zhang, L. Zhang, and H. Shen, "A super-resolution reconstruction algorithm for hyperspectral images," *Elsevier Sig. Proc.*, vol. 92, no. 9, pp. 2082–2096, Sept. 2012.

[8] J. Oliveira, M.A.T. Figueiredo, and J. Bioucas-Dias, "Parametric blur estimation for blind restoration of natural images: linear motion and out-of-focus," *IEEE Trans. Image Process.*, vol. 23, pp. 466–477, 2014.

[9] G. Chierchia, N. Pustelnik, J.-C. Pesquet, and B. Pesquet-Popescu, "An epigraphical convex optimization approach for multicomponent image restoration using non-local structure tensor," in *Proc. Int. Conf. Acoust., Speech Signal Process.*, Vancouver, Canada, May 2013.

[10] Q. Yuan, L. Zhang, and H. Shen, "Hyperspectral image denoising employing a spectral-spatial adaptive total variation model," *IEEE Trans. Geosci. Remote Sens.*, vol. 50, no. 10, pp. 3660 – 3677, Oct. 2012.

[11] Q. Cheng, H. Shen, L. Zhang, and P. Li, "Inpainting for remotely sensed images with a multichannel nonlocal total variation model," *IEEE Trans. Geosci. Remote Sens.*, vol. 52, no. 1, pp. 175–187, Jan. 2014.

[12] L. Rudin, S. Osher, and E. Fatemi, "Nonlinear total variation based noise removal algorithms," *Physica D*, vol. 60, no. 1-4, pp. 259–268, Nov. 1992.

[13] P. L. Combettes and J.-C. Pesquet, "Image restoration subject to a total variation constraint," *IEEE Trans. Image Process.*, vol. 13, no. 9, pp. 1213–1222, Sept. 2004.

[14] K. Bredies, K. Kunisch, and T. Pock, "Total generalized variation," *SIAM J. on Imaging Sci.*, vol. 3, no. 3, pp. 492–526, Sept. 2010.

[15] S. Ono and I. Yamada, "Second-order total generalized variation constraint," in *Proc. Int. Conf. Acoust., Speech Signal Process.*, Florence, Italy, May 4-9 2014.

[16] Y. Hu and M. Jacob, "Higher degree total variation (HDTV) regularization for image recovery," *IEEE Trans. Image Process.*, vol. 21, no. 5, pp. 2559–2571, May 2012.

[17] Y. Hu and M. Jacob, "Generalized higher degree total variation (HDTV) regularization," *IEEE Trans. Image Process.*, vol. 23, no. 6, pp. 2423–2435, June 2014.

[18] G. Gilboa and S. Osher, "Nonlocal operators with applications to image processing," *Multiscale Model. and Simul.*, vol. 7, no. 3, pp. 1005, 2009.

[19] C. Sutour, C.-A. Deledalle, and J.-F. Aujol, "Adaptive regularization of the NL-means: Application to image and video denoising," *IEEE Trans. Image Process.*, 2014, to appear.

[20] Z. Yang and M. Jacob, "Nonlocal regularization of inverse problems: a unified variational framework," *IEEE Trans. Image Process.*, vol. 22, no. 8, pp. 3192–3203, Aug. 2013.

[21] S. Mallat, *A wavelet tour of signal processing*, Academic Press, San Diego, USA, 1997.

[22] A. Benazza-Benyahia and J.-C. Pesquet, "Building robust wavelet estimators for multicomponent images using Stein's principle," *IEEE Trans. Image Process.*, vol. 14, no. 11, pp. 1814 – 1830, 2005.

[23] C. Chaux, L. Duval, A. Benazza-Benyahia, and J.-C. Pesquet, "A nonlinear Stein-based estimator for multichannel image denoising," *IEEE Trans. Signal Process.*, vol. 56, no. 8, pp. 3855 – 3870, 2008.

[24] C. Chaux, A. Benazza-Benyahia, J.-C. Pesquet, and Duval, "Wavelet transform for the denoising of multivariate images," in *Multivariate Image Processing*, C. Collet, J. Chanussot, and K. Chehdi, Eds., pp. 203–237. ISTE Ltd. and John Wiley & Sons Inc., 2010.

[25] L. M. Briceño-Arias, P. L. Combettes, J.-C. Pesquet, and N. Pustelnik, "Proximal algorithms for multicomponent image recovery problems," *J. Math. Imag. Vis.*, vol. 41, no. 1, pp. 3–22, Sept. 2011.

[26] A. Foi, V. Katkovnik, and K. Egiazarian, "Pointwise shape-adaptive DCT for high-quality denoising and deblocking of grayscale and color images," *IEEE Trans. Image Process.*, vol. 16, no. 5, pp. 1395–1411, May 2007.

[27] M. Aharon, M. Elad, and A. Bruckstein, "K-SVD: An algorithm for designing overcomplete dictionaries for sparse representation," *IEEE Trans. Signal Process.*, vol. 54, no. 11, pp. 4311–4322, Nov. 2006.

[28] M. Elad, M. A. T. Figueiredo, and Y. Ma, "On the role of sparse and redundant representations in image processing," *Proceedings of the IEEE*, vol. 98, no. 6, pp. 972–982, June 2010.

[29] X. Li, H. Shen, L. Zhang, H. Zhang, Q. Yuan, and G. Yang, "Recovering quantitative remote sensing products contaminated by thick clouds and shadows using multitemporal dictionary learning," *IEEE Trans. Geosci. Remote Sens.*, vol. 52, no. 11, pp. 7086–7098, Nov. 2014.

[30] K. Dabov, A. Foi, V. Katkovnik, and K. Egiazarian, "Image denoising by sparse 3D transform-domain collaborative filtering," *IEEE Trans. Image Process.*, vol. 16, no. 8, pp. 2080 – 2095, Aug. 2007.

[31] M. Maggioni, V. Katkovnik, K. Egiazarian, and A. Foi, "A nonlocal transform-domain filter for volumetric data denoising and reconstruction," *IEEE Trans. Image Process.*, vol. 22, no. 1, pp. 119 – 133, Jan. 2013.

[32] A. Danielyan, V. Katkovnik, and K. Egiazarian, "BM3D frames and variational image deblurring," *IEEE Trans. Image Process.*, vol. 21, no. 4, pp. 1715–1728, 2012.

[33] P. Blomgren and T.F. Chan, "Color TV: total variation methods for restoration of vector-valued images," *IEEE Trans. Image Process.*, vol. 7, no. 3, pp. 304–309, Mar. 1998.

[34] H. Attouch, G. Buttazzo, and G. Michaille, *Variational Analysis in Sobolev and BV Spaces: Applications to PDEs and Optimization*, MPS-SIAM Series on Optimization, 2006.

[35] C. Zach, T. Pock, and H. Bischof, "A duality based approach for realtime TV-L1 optical flow," in *Proc. DAGM Symposium*, Heidelberg, Germany, Sep. 12-14, 2007, pp. 214–223.

[36] V. Duval, J.-F. Aujol, and L. Vese, "Projected gradient based color image decomposition," in *Scale Space and Variational Methods in Computer Vision*, vol. 5567, pp. 295–306. Springer Verlag, 2009.

[37] S. Di Zenzo, "A note on the gradient of a multi-image," *Comput. Vis., Graph. and Image Process.*, vol. 33, no. 1, pp. 116–125, Jan. 1986.

[38] G. Sapiro and D. L. Ringach, "Anisotropic diffusion of multivalued images with applications to color filtering," *IEEE Trans. Image Process.*, vol. 5, no. 11, pp. 1582–1586, Nov. 1996.

[39] N. Sochen, R. Kimmel, and R. Malladi, "A general framework for low level vision," *IEEE Trans. Image Process.*, vol. 7, no. 3, pp. 310–318, Mar. 1998.

[40] J. Weickert, "Coherence-enhancing diffusion of colour images," *Image and Vision Computing*, vol. 17, no. 3-4, pp. 201 – 212, Mar. 1999.

[41] D. Tschumperlé and R. Deriche, "Constrained and unconstrained PDE's for vector image restoration," in *Scandinavian Conference on Image Analysis*, Bergen, Norway, Jun. 11-14, 2001.

[42] X. Bresson and T. F. Chan, "Fast dual minimization of the vectorial total variation norm and applications to color image processing," *Inverse Prob. Imaging*, vol. 2, no. 4, pp. 455–484, Nov. 2008.

[43] M. Jung, X. Bresson, T. F. Chan, and L. A. Vese, "Nonlocal Mumford-Shah regularizers for color image restoration," *IEEE Trans. Image Process.*, vol. 20, no. 6, pp. 1583–1598, June 2011.

[44] B. Goldluecke, E. Strekalovskiy, and D. Cremers, "The natural vectorial total variation which arises from geometric measure theory," *SIAM J. Imaging Sci.*, vol. 5, no. 2, pp. 537–563, 2012.

[45] S. Lefkimmiatis, A. Roussos, M. Unser, and P. Maragos, "Convex generalizations of total variation based on the structure tensor with applications to inverse problem," in *Scale-Space and Variational Methods in Computer Vision*, 2013, vol. 7893, pp. 48–60.

[46] D. C. Youla and H. Webb, "Image restoration by the method of convex projections. Part I - Theory," *IEEE Trans. Med. Imag.*, vol. 1, no. 2, pp. 81–94, Oct. 1982.

[47] H. J. Trussell and M. R. Civanlar, "The feasible solution in signal restoration," *IEEE Trans. Acous. Speech Signal Process.*, vol. 32, no. 2, pp. 201–212, Apr. 1984.

[48] P. L. Combettes, "Inconsistent signal feasibility problems: least-squares solutions in a product space," *IEEE Trans. Signal Process.*, vol. 42, no. 11, pp. 2955–2966, Nov. 1994.

[49] K. Kose, V. Cevher, and A. E. Cetin, "Filtered variation method for denoising and sparse signal processing," in *Proc. Int. Conf. Acoust., Speech Signal Process.*, Kyoto, Japan, Mar. 25-30, 2012, pp. 3329–3332.

Copyright (c) 2014 IEEE. Personal use is permitted. For any other purposes, permission must be obtained from the IEEE by emailing pubs-permissions@ieee.org.

This is the author's version of an article that has been published in this journal. Changes were made to this version by the publisher prior to publication.
The final version of record is available at http://dx.doi.org/10.1109/TIP.2014.2364141

[50] T. Teuber, G. Steidl, and R. H. Chan, "Minimization and parameter estimation for seminorm regularization models with I-divergence constraints," *Inverse Problems*, vol. 29, pp. x+29, 2013.
[51] C. Studer, W. Goldstein, T. Yin, and R. G. Baraniuk, "Democratic representations," Jan. 2014, Preprint: http://arxiv.org/pdf/1401.3420v1.pdf.
[52] J.-B. Hiriart-Urruty and C. Lemaréchal, *Convex analysis and minimization algorithms, Part I : Fundamentals*, vol. 305 of *Grundlehren der mathematischen Wissenschaften*, Springer-Verlag, Berlin, Heidelberg, N.Y., 2nd edition, 1996.
[53] P. Valero, S. Salembier and J. Chanussot, "Hyperspectral image representation and processing with binary partition trees," *IEEE Trans. Image Process.*, vol. 22, no. 4, pp. 1430–1443, Apr. 2013.
[54] R. Molina, J. Nunez, F. J. Cortijo, and J. Mateos, "Image restoration in astronomy: A Bayesian perspective," *IEEE Signal Proc. Mag.*, vol. 18, no. 2, pp. 11–29, Mar. 2001.
[55] C. Vonesch, F. Aguet, J.-L. Vonesch, and M. Unser, "The colored revolution of bioimaging," *IEEE Signal Proc. Mag.*, vol. 23, no. 3, pp. 20–31, May 2006.
[56] K. Bernard, Y. Tarabalka, J. Angulo, J. Chanussot, and J. A. Benediktsson, "Spectralspatial classification of hyperspectral data based on a stochastic minimum spanning forest approach," *IEEE Trans. Image Process.*, vol. 21, no. 4, pp. 2008 – 2021, Apr. 2012.
[57] D. Tschumperlé and R. Deriche, "Vector-valued image regularization with pdes: A common framework for different applications," *IEEE Trans. Pattern Anal. Match. Int.*, vol. 27, no. 4, pp. 506–517, Apr. 2005.
[58] J. Martin-Herrero, "Anisotropic diffusion in the hypercube," *IEEE Trans. Geosci. Remote Sens.*, vol. 45, no. 5, pp. 1386–1398, May 2007.
[59] R. Mendez-Rial, M. Calvino-Cancela, and J. Martin-Herrero, "Accurate implementation of anisotropic diffusion in the hypercube," *IEEE Geosci. Remote Sens. Lett.*, vol. 7, no. 4, pp. 870–874, 2010.
[60] T. Lin and S. Bourennane, "Survey of hyperspectral image denoising methods based on tensor decompositions," *EURASIP J. Advances Sig. Proc.*, vol. 186, 2013.
[61] E. J. Candès, X Li, Y. Ma, and J. Wright, "Robust principal component analysis?," *J. ACM*, vol. 58, no. 3, pp. 11:1–11:37, May 2011.
[62] D. Hsu, S. M. Kakade, and T. Zhang, "Robust matrix decomposition with sparse corruptions," *IEEE Trans. Inform. Theory*, vol. 57, no. 11, pp. 7221–7234, Nov. 2011.
[63] G. Ely, S. Aeron, and E. L. Miller, "Exploiting structural complexity for robust and rapid hyperspectral imaging," in *Proc. Int. Conf. Acoust., Speech Signal Process.*, Vancouver, Canada, June 2013.
[64] N. Dobigeon, S. Moussaoui, M. Coulon, J.-Y. Tourneret, and A. O. Hero, "Joint bayesian endmember extraction and linear unmixing for hyperspectral imagery," *IEEE Trans. Signal Process.*, vol. 57, no. 11, pp. 4355–4368, 2009.
[65] E. Chouzenoux, M. Legendre, S. Moussaoui, and J. Idier, "Fast constrained least squares spectral unmixing using primal-dual interior point optimization," *IEEE Journal of Selected Topics in Applied Earth Observations and Remote Sensing*, pp. 59–69, 2013.
[66] W.-K Ma, J. Bioucas-Dias, T.-H. Chan, N. Gillis, P. Gader, A. Plaza, Ambikapathi A., and C.-Y. Chi, "A signal processing perspective on hyperspectral unmixing," *IEEE Trans. Signal Process.*, 2014, to appear.
[67] G. W. Stewart, "On the early history of the singular value decomposition," *SIAM Review*, vol. 35, no. 4, pp. 551–566, 1993.
[68] S. Ono and M. Yamada, "A convex regularizer for reducing color artifact in color image recovery," in *CVPR*, Portland, USA, June 2013.
[69] J.-F. Aujol, "Some first-order algorithms for total variation based image restoration," *J. Math. Imag. Vis.*, vol. 34, no. 3, pp. 307–327, July 2009.
[70] A. Buades, B. Coll, and J. Morel, "A review of image denoising algorithms, with a new one," *Multiscale Model. and Simul.*, vol. 4, no. 2, pp. 490–530, 2005.
[71] A. Foi and G. Boracchi, "Foveated self-similarity in nonlocal image filtering," in *Proc. SPIE Electronic Imaging 2012, Human Vision and Electronic Imaging XVII*, Burlingame (CA), USA, Jan. 2012, vol. 8291.
[72] G. Gilboa and S. Osher, "Nonlocal linear image regularization and supervised segmentation," *Multiscale Model. and Simul.*, vol. 6, no. 2, pp. 595–630, 2007.
[73] E. Van Den Berg and M. P. Friedlander, "Probing the Pareto frontier for basis pursuit solutions," *SIAM J. Sci. Comput.*, vol. 31, no. 2, pp. 890–912, Nov. 2008.
[74] A. Quattoni, X. Carreras, M. Collins, and T. Darrell, "An efficient projection for $\ell_{1,\infty}$ regularization," in *International Conference on Machine Learning*, Montreal, Quebec, Jun. 14-18, 2009, pp. 857–864.
[75] G. Chierchia, N. Pustelnik, J.-C. Pesquet, and B. Pesquet-Popescu, "Epigraphical projection and proximal tools for solving constrained convex optimization problems," *Signal Image Video Process.*, 2014, to appear.
[76] S. Harizanov, J.-C. Pesquet, and G. Steidl, "Epigraphical projection for solving least squares Anscombe transformed constrained optimization problems," in *Scale-Space and Variational Methods in Computer Vision*, 2013, vol. 7893, pp. 125–136.
[77] M Tofighi, K. Kose, and A. E. Cetin, "Signal reconstruction framework based on Projections onto Epigraph Set of a Convex cost function (PESC)," 2014, preprint.
[78] R. T. Rockafellar and R. J.-B. Wets, *Variational analysis*, Springer-Verlag, 2004.
[79] I. Daubechies, M. Defrise, and C. De Mol, "An iterative thresholding algorithm for linear inverse problems with a sparsity constraint," *Comm. Pure Applied Math.*, vol. 57, no. 11, pp. 1413–1457, Nov. 2004.
[80] C. Chaux, P. L. Combettes, J.-C. Pesquet, and V. R. Wajs, "A variational formulation for frame-based inverse problems," *Inverse Problems*, vol. 23, no. 4, pp. 1495–1518, Jun. 2007.
[81] P. L. Combettes and J.-C. Pesquet, "A Douglas-Rachford splitting approach to nonsmooth convex variational signal recovery," *IEEE J. Selected Topics Signal Process.*, vol. 1, no. 4, pp. 564–574, Dec. 2007.
[82] M. Figueiredo, R. Nowak, and S. Wright, "Gradient projection for sparse reconstruction: application to compressed sensing and other inverse problems," *IEEE J. Sel. Topics Signal Process.: Special Issue on Convex Optim. Methods for Signal Process.*, vol. 5981, no. 4, pp. 586–598, Dec. 2007.
[83] A. Beck and M. Teboulle, "A fast iterative shrinkage-thresholding algorithm for linear inverse problems," *SIAM J. Imaging Sci.*, vol. 2, no. 1, pp. 183–202, 2009.
[84] M. Fornasier and C.-B. Schönlieb, "Subspace correction methods for total variation and ℓ_1-minimization," *IMA J. Numer. Anal.*, vol. 47, no. 8, pp. 3397–3428, 2009.
[85] G. Steidl and T. Teuber, "Removing multiplicative noise by Douglas-Rachford splitting methods," *J. Math. Imag. Vis.*, vol. 36, no. 3, pp. 168–184, 2010.
[86] P. L. Combettes and J.-C. Pesquet, "Proximal splitting methods in signal processing," in *Fixed-Point Algorithms for Inverse Problems in Science and Engineering*, H. H. Bauschke, R. S. Burachik, P. L. Combettes, V. Elser, D. R. Luke, and H. Wolkowicz, Eds., pp. 185–212. Springer-Verlag, New York, 2011.
[87] J.-C. Pesquet and N. Pustelnik, "A parallel inertial proximal optimization method," *Pac. J. Optim.*, vol. 8, no. 2, pp. 273–305, Apr. 2012.
[88] G. Chen and M. Teboulle, "A proximal-based decomposition method for convex minimization problems," *Math. Program.*, vol. 64, pp. 81–101, 1994.
[89] E. Esser, X. Zhang, and T. Chan, "A general framework for a class of first order primal-dual algorithms for convex optimization in imaging science," *SIAM J. Imaging Sci.*, vol. 3, no. 4, pp. 1015–1046, 2010.
[90] A. Chambolle and T. Pock, "A first-order primal-dual algorithm for convex problems with applications to imaging," *J. Math. Imag. Vis.*, vol. 40, no. 1, pp. 120–145, 2011.
[91] L. M. Briceño-Arias and P. L. Combettes, "A monotone + skew splitting model for composite monotone inclusions in duality," *SIAM J. Opt.*, vol. 21, no. 4, pp. 1230–1250, 2011.
[92] P. L. Combettes and J.-C. Pesquet, "Primal-dual splitting algorithm for solving inclusions with mixtures of composite, Lipschitzian, and parallel-sum type monotone operators," *Set-Valued Var. Anal.*, vol. 20, no. 2, pp. 307–330, Jun. 2012.
[93] B. C. Vũ, "A splitting algorithm for dual monotone inclusions involving cocoercive operators," *Adv. Comput. Math.*, vol. 38, no. 3, pp. 667–681, Apr. 2013.
[94] L. Condat, "A primal-dual splitting method for convex optimization involving Lipschitzian, proximable and linear composite terms," *J. Optim. Theory Appl.*, vol. 158, no. 2, pp. 460–479, Aug. 2012.
[95] P. Chen, J. Huang, and X. Zhang, "A primal-dual fixed point algorithm for convex separable minimization with applications to image restoration," *Inverse Problems*, vol. 29, no. 2, 2013.
[96] N. Komodakis and J.-C. Pesquet, "Playing with duality: An overview of recent primal-dual approaches for solving large-scale optimization problems," 2014, http://arxiv.org/abs/1406.5429.
[97] J. J. Moreau, "Proximité et dualité dans un espace hilbertien," *Bull. Soc. Math. France*, vol. 93, pp. 273–299, 1965.
[98] J. Eckstein and D. P. Bertsekas, "On the Douglas-Rachford splitting method and the proximal point algorithm for maximal monotone operators," *Mathematical Programming*, vol. 55, pp. 293–318, 1992.
[99] S. Setzer, G. Steidl, and T. Teuber, "Deblurring Poissonian images by split Bregman techniques," *J. Visual Communication and Image Representation*, vol. 21, no. 3, pp. 193–199, Apr. 2010.

Copyright (c) 2014 IEEE. Personal use is permitted. For any other purposes, permission must be obtained from the IEEE by emailing pubs-permissions@ieee.org.

This is the author's version of an article that has been published in this journal. Changes were made to this version by the publisher prior to publication.
The final version of record is available at http://dx.doi.org/10.1109/TIP.2014.2364141

[100] M. V. Afonso, J. M. Bioucas-Dias, and M. A. T. Figueiredo, "An augmented Lagrangian approach to the constrained optimization formulation of imaging inverse problems," *IEEE Trans. Image Process.*, vol. 20, no. 3, pp. 681–695, Mar. 2011.
[101] J. Eckstein, "Parallel alternating direction multiplier decomposition of convex programs," *J. Optim. Theory Appl.*, vol. 80, no. 1, pp. 39–62, 1994.
[102] P. L. Combettes and J.-C. Pesquet, "A proximal decomposition method for solving convex variational inverse problems," *Inverse Problems*, vol. 24, no. 6, Dec. 2008.
[103] M. V. Afonso, J. M. Bioucas-Dias, and M. A. T. Figueiredo, "Fast image recovery using variable splitting and constrained optimization," *IEEE Trans. Image Process.*, vol. 19, no. 9, pp. 2345–2356, 2010.
[104] N. Pustelnik, J.-C. Pesquet, and C. Chaux, "Relaxing tight frame condition in parallel proximal methods for signal restoration," *IEEE Trans. Signal Process.*, vol. 60, no. 2, pp. 968–973, Feb. 2012.
[105] G. Peyré and J. Fadili, "Group sparsity with overlapping partition functions," in *Proc. Eur. Sig. and Image Proc. Conference*, Barcelona, Spain, Aug. 29 – Sept. 2, 2011.
[106] P. Weiss, L. Blanc-Féraud, and G. Aubert, "Efficient schemes for total variation minimization under constraints in image processing," *SIAM J. Sci. Comput.*, vol. 31, no. 3, pp. 2047–2080, Apr. 2009.
[107] J. M. Fadili and G. Peyré, "Total variation projection with first order schemes," *IEEE Trans. Image Process.*, vol. 20, no. 3, pp. 657–669, Mar. 2011.
[108] L. Condat and S. Mosaddegh, "Joint demosaicking and denoising by total variation minimization," in *Proc. Int. Conf. Image Process.*, Orlando, USA, Sept. 2012.
[109] L. Condat, "A generic proximal algorithm for convex optimization - application to total variation minimization," *IEEE Signal Proc. Letters*, vol. 21, no. 8, pp. 1054–1057, Aug. 2014.
[110] L. Condat, "Fast projection onto the simplex and the l1 ball," 2014, http://hal.archives-ouvertes.fr/hal-01056171.

Giovanni Chierchia received the engineering degree in computer science from University of Naples Federico II, Italy, in 2010. From 2010 to 2011, he worked as research engineer at Institut Mines-Télécom, Télécom ParisTech, CNRS LTCI, Paris, France, and is currently a Ph.D. student in the same institution. His research interests are in constrained convex optimization, focusing on its applications to image restoration, image forgery detection, video coding, and machine learning.

Nelly Pustelnik was born in Sarlat-la-Canéda, France. She received the Ph.D. degree in signal and image processing from the Université Paris-Est Marne-la-Vallée, France, in 2010. From 2010 to 2011, she was a Postdoctoral research associate with the Laboratoire IMS, Université de Bordeaux, France, working on the topic of tomographic reconstruction from a limited number of projections. Since 2012, she is a CNRS researcher in the Signal Processing Team of the Laboratoire de Physique de l'ENS de Lyon. Her activity is focused on inverse problems, non-smooth convex optimization, mode decomposition, and texture analysis.

Béatrice Pesquet-Popescu (SM'06, F'13) received the engineering degree in telecommunications from the "Politehnica" Institute in Bucharest in 1995 (highest honours) and the Ph.D. degree from the Ecole Normale Supérieure de Cachan in 1998. In 1998, she was a Research and Teaching Assistant with Université Paris XI, Paris. In 1999, she joined Philips Research France, Suresnes, France, where she worked for two years as a Research Scientist, then as a Project Leader, in scalable video coding. Since Oct. 2000 she is with Télécom ParisTech (formerly, ENST), first as an Associate Professor, and since 2007 as a Professor, Head of the Multimedia Group. She is the Head of the UBIMEDIA common research laboratory between Alcatel-Lucent and Institut Télécom. Her current research interests are in source coding, scalable, robust and distributed video compression and sparse representations.

Dr. Pesquet-Popescu was an EURASIP BoG member (2003-2010), and an IEEE Signal Processing Society IVMSP TC member and MMSP TC associate member. She serves as an Associate Editor for IEEE Trans. on Image Processing, IEEE Trans. on Multimedia, IEEE Trans. on CSVT, Elsevier Image Communication, and Hindawi Int. J. Digital Multimedia Broadcasting journals and was till 2010 an Associate Editor for Elsevier Signal Processing. She was a Technical Co-Chair for the PCS2004 conference, and General Co-Chair for IEEE SPS MMSP2010, EUSIPCO 2012, and IEEE SPS ICIP 2014 conferences. Beatrice Pesquet-Popescu is a recipient of the "Best Student Paper Award" in the IEEE Signal Processing Workshop on Higher-Order Statistics in 1997, of the Bronze Inventor Medal from Philips Research and in 1998 she received a "Young Investigator Award" granted by the French Physical Society. She holds 23 patents in wavelet-based video coding and has authored more than 290 book chapters, journal and conference papers in the field. In 2006, she was the recipient, together with D. Turaga and M. van der Schaar, of the IEEE Trans. on Circuits and Systems for Video Technology "Best Paper Award".

Jean-Christophe Pesquet (S'89–M'91–SM'99–F'12) received the engineering degree from Supélec, Gif-sur-Yvette, France, in 1987, the Ph.D. degree from the Université Paris-Sud (XI), Paris, France, in 1990, and the Habilitation à Diriger des Recherches from the Université Paris-Sud in 1999.

From 1991 to 1999, he was a Maître de Conférences at the Université Paris-Sud, and a Research Scientist at the Laboratoire des Signaux et Systèmes, Centre National de la Recherche Scientifique (CNRS), Gif-sur-Yvette. He is currently a Professor (classe exceptionnelle) with Université de Paris-Est Marne-la-Vallée, France, and the Deputy Director of the Laboratoire d'Informatique of the university (UMR–CNRS 8049).

Copyright (c) 2014 IEEE. Personal use is permitted. For any other purposes, permission must be obtained from the IEEE by emailing pubs-permissions@ieee.org.